



## Article

\*Now at: Department of Geosciences, University of Tübingen, Tübingen, Germany.

**Cite this article:** Wild CT et al. (2024). Rift propagation signals the last act of the Thwaites Eastern Ice Shelf despite low basal melt rates. *Journal of Glaciology* 70, e21, 1–18. <https://doi.org/10.1017/jog.2024.64>

Received: 27 February 2024

Revised: 6 August 2024

Accepted: 11 August 2024

**Keywords:**




Antarctic glaciology; crevasses; ice/ocean interactions; ice-shelf break-up; melt – basal

**Corresponding author:**

Christian T. Wild;

Email: [christian.wild@uni-tuebingen.de](mailto:christian.wild@uni-tuebingen.de)

# Rift propagation signals the last act of the Thwaites Eastern Ice Shelf despite low basal melt rates

Christian T. Wild<sup>1,\*</sup> , Samuel B. Kachuck<sup>2</sup> , Adrian Luckman<sup>3</sup> , Karen E. Alley<sup>4</sup> , Meghan A. Sharp<sup>1</sup> , Haylee Smith<sup>1</sup> , Scott W. Tyler<sup>5</sup> , Christopher Kratt<sup>5</sup> , Tiago S. Dotto<sup>6</sup> , Daniel Price<sup>7</sup> , Keith W. Nicholls<sup>8</sup> , Suzanne L. Bevan<sup>3</sup> , Gabriela Collao-Barrios<sup>9</sup> , Atsuhiko Muto<sup>10</sup> , Martin Truffer<sup>11</sup> , Ted A. Scambos<sup>12</sup> , Karen J. Heywood<sup>13</sup> , Erin C. Pettit<sup>1</sup>  and the TARSAN team

<sup>1</sup>College of Earth, Ocean, and Atmospheric Sciences, Oregon State University, Corvallis, OR, USA; <sup>2</sup>Climate and Space Sciences and Engineering, University of Michigan, Ann Arbor, MI, USA; <sup>3</sup>Department of Geography, Faculty of Science and Engineering, Swansea University, Swansea, UK; <sup>4</sup>Centre for Earth Observation Science, University of Manitoba, Winnipeg, Manitoba, Canada; <sup>5</sup>Department of Geological Sciences and Engineering, University of Nevada, Reno, NV, USA; <sup>6</sup>National Oceanography Centre, Southampton, UK; <sup>7</sup>Gateway Antarctica, School of Earth & Environment, University of Canterbury, Christchurch, New Zealand; <sup>8</sup>British Antarctic Survey, Cambridge, UK; <sup>9</sup>National Snow and Ice Data Center, CIRES, University of Colorado Boulder, Boulder, CO, USA; <sup>10</sup>Department of Earth and Environmental Science, Temple University, Philadelphia, PA, USA; <sup>11</sup>Geophysical Institute and Department of Physics, University of Alaska Fairbanks, Fairbanks, AK, USA; <sup>12</sup>Earth Science and Observation Center, CIRES, University of Colorado Boulder, Boulder, CO, USA and <sup>13</sup>Centre for Ocean and Atmospheric Sciences, School of Environmental Sciences, University of East Anglia, Norwich, UK

**Abstract**

Rift propagation, rather than basal melt, drives the destabilization and disintegration of the Thwaites Eastern Ice Shelf. Since 2016, rifts have episodically advanced throughout the central ice-shelf area, with rapid propagation events occurring during austral spring. The ice shelf's speed has increased by ~70% during this period, transitioning from a rate of 1.65 m d<sup>-1</sup> in 2019 to 2.85 m d<sup>-1</sup> by early 2023 in the central area. The increase in longitudinal strain rates near the grounding zone has led to full-thickness rifts and melange-filled gaps since 2020. A recent sea-ice break out has accelerated retreat at the western calving front, effectively separating the ice shelf from what remained of its northwestern pinning point. Meanwhile, a distributed set of phase-sensitive radar measurements indicates that the basal melting rate is generally small, likely due to a widespread robust ocean stratification beneath the ice–ocean interface that suppresses basal melt despite the presence of substantial oceanic heat at depth. These observations in combination with damage modeling show that, while ocean forcing is responsible for triggering the current West Antarctic ice retreat, the Thwaites Eastern Ice Shelf is experiencing dynamic feedbacks over decadal timescales that are driving ice-shelf disintegration, now independent of basal melt.

**1. Introduction**

The evolution of ice shelves, which are the floating extensions of glaciers into the ocean, plays a crucial role in ice-sheet evolution. Observations of ice-shelf collapses around Antarctica have highlighted the subsequent retreat of grounding zones (Rack and Rott, 2004; Konrad and others, 2018) and the associated acceleration of ice discharge into the ocean (Scambos and others, 2004; Pritchard and others, 2009). This is particularly concerning for glaciers situated in West Antarctica, where modeling studies suggest irreversible feedback mechanisms may operate along retrograde beds (Joughin and others, 2014; Seroussi and others, 2017) and on newly exposed ice cliffs (Pollard and others, 2015; Crawford and others, 2021). For the Amundsen Sea sector glaciers, intrusion of warm ocean water (Schmidtke and others, 2014) has caused basal melting and significant thinning of ice shelves near their grounding zones (Jenkins and others, 2018), widespread retreat of their margins (MacGregor and others, 2012) and ultimately ice-mass loss (Sutterley and others, 2014). Ice shelves provide resistance to the flow of upstream grounded ice as they deform against lateral confinements and seafloor pinning points at their bases (Gudmundsson, 2013). As the ice shelves thin in response to warm ocean water, this buttressing is reduced, leading to increasing rates of ice flow into the ocean and sea-level rise.

The Thwaites Eastern Ice Shelf is laterally unconfined, and primarily transmits buttressing stresses from a narrow pinning point at its northern end. This pinning point consists of a larger eastern and a smaller western ice rumple, but ongoing ice-shelf thinning is expected to lead to their detachment within the next decade (Wild and others, 2022). Furthermore, a strong stratification of the water beneath the ice–ocean interface suppresses rapid basal melting despite high thermal forcing (Dotto and others, 2022; Davis and others, 2023; Schmidt and

© The Author(s), 2024. Published by Cambridge University Press on behalf of International Glaciological Society. This is an Open Access article, distributed under the terms of the Creative Commons Attribution licence (<http://creativecommons.org/licenses/by/4.0/>), which permits unrestricted re-use, distribution and reproduction, provided the original article is properly cited.

[cambridge.org/jog](https://cambridge.org/jog)



others, 2023), indicating that current ice-shelf thinning is primarily due to dynamic processes rather than melting from beneath. This distinction is pivotal, as it opens the door to the possibility of a new dynamical regime (Benn and others, 2022). In this study, we propose a method for segregating thinning into distinct melt and dynamic components. Further modeling research also suggests that the ice shelf has depleted its buttressing capacity (Gudmundsson and others, 2023), suggesting that Thwaites' last remaining ice shelf has lost its structural integrity and is nearing the end of its life.

The history of the Thwaites Eastern Ice Shelf is intricately linked to the neighboring Thwaites Western Glacier Tongue, and many present-day surface features on the Eastern Ice Shelf are the outcome of their past interactions. In the early 2000s, a strongly compressive shear margin between them led to an acceleration of the Eastern Ice Shelf, as it was dragged on its western side by the faster-moving western ice (Alley and others, 2021). In 2007, the formation of large fractures along their shear margin marked the beginning of the disintegration of the Western Glacier Tongue. The shear margin continued to deteriorate over the subsequent years, leading to a significant reduction in the Thwaites Eastern Ice Shelf velocity as the connection was lost by 2008–09 (Tinto and Bell, 2011; MacGregor and others, 2012; Miles and others, 2020). Consequently, the Eastern Ice Shelf experienced an earlier maximum speed between 2005 and 2007, followed by a swift deceleration in 2009 due to the disappearance of its western shear margin (Benn and others, 2022). The Western Glacier Tongue experienced nearly complete disintegration following these events, with major calving events in the summer of 2012–13, and has had little control on the velocity of the Eastern Ice Shelf since this disintegration. The early 2000s Eastern Ice Shelf acceleration led to the formation of a swarm of crevasses that began to emerge just downstream of the grounding zone ~2005. Since the loss of the Western Glacier Tongue, these remnant crevasses have been transported with the ice flow and are gradually being filled by snow accumulation, ice creep and longitudinal compression (Alley and others, 2021).

With Thwaites Glacier now freely draining through its main trunk into the embayment left by the former Western Glacier Tongue, the Eastern Ice Shelf has developed distinct flow dynamics, primarily influenced by its northern pinning point. Initially, shearing across this point imparted a strong backstress on the Eastern Ice Shelf. As time passed, this shear zone underwent a counterclockwise rotation as the Eastern Ice Shelf adjusted to the diminished influence of the Western Glacier Tongue's lateral drag (Wild and others, 2022). Remarkably, despite the considerable weakening of the stress along the pinning ice rumple, the ice-flow speed in the central ice shelf remained fairly steady from 2015 to 2019. During this time, full-thickness rifts emerged from the shear zone and extended toward the central region of the ice shelf (Benn and others, 2022). From 2019 to 2022, the ice-shelf speed accelerated due to diminishing support from the pinning point. This acceleration was accompanied by the development of extensive rifts within the now nearly flow-parallel shear zone, effectively disconnecting the remaining ice-shelf area structurally from its pinning point (Benn and others, 2022). Extensive field data of this dynamic system were collected by the International Thwaites Glacier Collaboration's TARSAN project, around Cavity Camp (Fig. 1), named for its central location above the ocean cavity beneath the ice.

In this paper, we demonstrate how the impending disintegration of the Thwaites Eastern Ice Shelf, which was initiated by ocean melting likely in the first few kilometers downstream of the grounding zone (Clark and others, 2024), has transitioned to a regime dominated by ice dynamics and fracture, demonstrated by significant structural changes to the shelf in the

presence of low basal melt rates. We integrate field and remotely sensed data with damage modeling to construct a comprehensive picture of the current structural integrity of the ice shelf. Time series of Sentinel-1 imagery (Supplementary Video 1A) depict the episodic propagation of rifts across its central zone since 2016 and the recent activation of its western calving front. We also track the opening of full-thickness rifts along the retreating grounding zone, and use damage modeling to show that rift openings compensate fully for the strain expected from the shelf's acceleration. Autonomous phase-sensitive radar (ApRES) data indicate low-to-moderate ice-shelf melting, with vertical strain patterns closely linked to active rift zones. The results, coupled with damage modeling experiments conducted both with and without considering the relatively minor basal melt rates, show that the current disintegration of the ice shelf is mainly driven by dynamic processes resulting from the unpinning of the ice shelf.

## 2. Methods

### 2.1 Remote sensing

#### 2.1.1 Monitoring rift formation and propagation remotely

We used the Sentinel-1 dual satellite synthetic-aperture radar (SAR) system (Sentinel-1A and 1B) operating at C-band (5.4 GHz/5.6 cm) to monitor the Thwaites Eastern Ice Shelf between 2014 and 2024. Each active microwave sensor acquires images consistently every 12 d, resulting in a 6 d repeat-pass interval, apart from the periods prior to September 2016 and after December 2021 when only Sentinel-1A was operational. Images are acquired regardless of polar night and cloud cover, ensuring uninterrupted data acquisition compared with optical imaging systems. We used a high-resolution interferometric wide-swath mode product with a single HH polarization and a spatial resolution of 10 m. HH polarization refers to horizontally transmitted and horizontally received polarization of the radar signal. For the image analysis, we enhanced the contrast of each individual Sentinel-1 image through histogram equalization by using the cumulative distribution function from the 'exposure' module of the skimage package within the scikit-image library in Python (van der Walt and others, 2014), which leverages the probability distribution of pixel intensities within the image. From the processed images, we compiled two videos showing both the regional-scale evolution of the Thwaites Eastern Ice Shelf and the local evolution of a number of rifts growing across its central part (Supplementary materials). We present processed Sentinel-1 images for key dates to show rifting and calving events.

From these enhanced images, we manually identified and marked the starting and ending coordinates of the surface expressions of five large fractures, which have been growing in the central ice-shelf area since 2016, and two fracture features forming at the grounding zone since April 2021. The two features along the grounding zone have collapsed snow bridges revealing patches of ocean water and confirming that they penetrate the full ice thickness. Recent Sentinel-1 SAR images indicate that the collapse of snow bridges has also begun at the widest parts of the five large fractures extending into the central ice-shelf area. We therefore identify all of these features as full-thickness rifts, and refer to them as rifts throughout the paper.

Errors in our manual rift-tip measurements could stem from picking inaccuracies or snow bridging, which obscures the beginning and end points of the rift. We focused on the increase in length of the predominant rift, labeled as the dark blue rift in Figure 1, and applied piecewise linear fitting to assess the uncertainty in the rift length. This is based on the assumption that high-frequency variations in the rift length (in particular negative

deviations) are a consequence of picking inaccuracy. During the initial phase ( $0.2 \text{ km a}^{-1}$  in 2016), the residual std dev. around this trend was  $\pm 0.16 \text{ km}$ , with a rift length ranging between 1.1 and 1.5 km. Subsequent rapid growth increased the uncertainty to  $\pm 0.19 \text{ km}$ . Enhanced picking accuracy and continued rift lengthening led to reduced uncertainties before and during the second rift growth between mid- and late-2017 ( $\pm 0.14 \text{ km}$ ), dropping to  $\pm 0.17 \text{ km}$  in the third phase between mid- and late-2018, before decreasing to  $\pm 0.09 \text{ km}$  during a stable phase in 2019. Since February 2020, the blue rift has steadily lengthened at a rate of  $0.4 \text{ km a}^{-1}$ , accompanied by an accuracy of  $\pm 0.39 \text{ km}$ . We attribute the increasing uncertainty in the final phase to the rift penetrating into an area of thicker ice, which smoothens out the surface depression over a wider area and obscures its tip in the satellite imagery.

### 2.1.2 Surface velocity fields from feature tracking

We derived surface velocity fields from the Sentinel-1 archive, over the same time period as the rift tracking (Section 2.1.1) applying standard feature/speckle tracking techniques (e.g. Luckman and others, 2015). Our feature tracking window size was  $416 \times 128$  pixels, which equated to  $\sim 1 \text{ km}$  in range and azimuth, and we spatially filtered each velocity map using the signal-to-noise ratio and a local variability threshold. We sampled the velocity field at  $50 \times 10$  pixels before geocoding to the Antarctic Polar Stereographic projection (EPSG:3031) at 100 m resolution using the REMA mosaic DEM (Howat and others, 2019) gap-filled by Bedmap2 surface topography data (Fretwell and others, 2013). We combined velocity maps into 3 monthly mean fields by averaging. Strain rates were calculated from these mean velocity maps in a  $3 \times 3$  neighborhood. We extracted velocity and strain data for the Hovmöller plots along flowlines derived from the mean velocity field for the whole of 2021, targeting the basal channel, Cavity Camp, and the shear zone.

## 2.2 In situ data

### 2.2.1 Measuring basal melting and vertical strain with ApRES

We measured basal melting and vertical strain using an ApRES system. The instrument transmits an electromagnetic chirp sweeping linearly from 200 to 400 MHz over 1 s (Nicholls and others, 2015). Within a discrete burst, we gathered 20 chirps every 10 min and subsequently recorded the burst average. ApRES were used in two modes: repeat-visit, for surveying multiple sites across the ice shelf, and continuous, to capture the ongoing evolution of strain-rate variability and basal melting specifically at Cavity Camp (Fig. 1). We further processed the data using the phase-coherent processing chain described by Brennan and others (2014) and Nicholls and others (2015). To determine internal-layer displacement, we cross-correlated internal layers from repeat visits at each site. We analyzed 8 m data chunks without overlap and retained those internal reflectors beneath the 50 m firn layer that exhibited over 90% coherence in phase between returns. A linear fit was then applied to the vertical displacement of these reflectors to estimate the depth of the ice base resulting solely from strain-induced deformation. This allowed us to quantify the accuracy of the determined ice-base shift with the RMSE of the linear regression used to fit the internal layer displacement. By employing this technique, we effectively separated changes in observed ice thickness attributed to strain and melting and obtained basal melt rates that remained unaffected by horizontal ice divergence, surface accumulation or firn compaction (Corr and others, 2002).

To capture the temporal changes in basal melt rates and strain deformation, we deployed an ApRES unit at Cavity Camp (Fig. 1). It remained operational from 16 January 2020 to 23 March 2020,

and was subsequently reinstalled on 11 January 2022, continuing to operate until 5 August 2022. The complete data collection period spans 274 d, with the ApRES recording data at 10 min intervals. We processed the data using a 3 h rolling window at 60 d intervals with 20 d overlaps, following the analysis by Vaňková and others (2020). For the continuous ApRES record at Cavity Camp, we selected a representative depth range near the ice base to calculate the non-melt strain-component time series. The chosen reference layer must be close to the ice base to experience the same strain deformation as the ice-ocean interface but distant enough to prevent spectral leakage of the basal return. We identified this depth range from the mean vertical strain profile of internal reflectors to be between 200 and 250 m depth below the ice-shelf surface (Figs 5b and S1). By tracking the vertical displacement of this reference layer and the basal return over time, we defined the melt rate as the difference between these two time series. The outlier correction involved identifying values in both the reference layer displacement and the basal return displacement that exceed the overall mean plus 1 std dev., adjusting periods with at least two consecutive outliers by subtracting their mean. This method preserves any temporal variability within the record.

We employed the software package developed by Grinsted and others (2004), to conduct a continuous wavelet transform of the resulting basal melt time series and the non-melt signal. Continuous wavelet analysis provides a time-frequency representation of the data, allowing us to observe how signal patterns evolve over time at different frequencies. Unlike Fourier analysis, which integrates information over the entire time series, wavelet analysis captures transient features and variations in frequency content, offering a more nuanced view of the time-series data. Statistical significance is tested using standard Monte Carlo methods.

Basal melt rates beneath the Eastern Ice Shelf exhibited significant spatial variability (Figs 3a and S2). However, it remained uncertain whether this variability reflects true spatial differences in melting or arises from temporal biases in repeat visits. Our 46 site revisits occurred, on average, every 12 d. To mitigate temporal biases, we further analyzed the continuous ApRES record at Cavity Camp. We determined a representative time span, ranging from 1 h to 31 d, to effectively capture basal melt rates without introducing temporal bias. We then plotted the temporal averages and std devs. of basal melting against the number of days between theoretical repeat visits (Fig. S3). This resulted in a sensitivity curve showing the variability of a value versus the time between measurements. For measurement intervals that are longer than 3 d, shorter lengths tend to slightly overestimate, and longer tend to slightly underestimate, the melt rate. For 2022 this error is  $<10\%$ , and for 2020, it is  $\sim 25\%$  of the total basal melt rate. Longer durations between repeat visits closely reflect the long-term basal melting. With repeat visits occurring between 6 and 22 d, our measurements closely represent long-term mean values, suggesting that spatial variability in basal melting is primarily driven by factors other than the duration between repeat visits, such as variability of local ice thickness (inset in Fig. 3b).

### 2.2.2 GNSS observations at Cavity Camp

Global Navigation Satellite Systems (GNSS) receivers were part of a larger geophysical observatory installed at two nearby locations on the ice shelf (Automated Meteorology-Ice Geophysical Observation System; Scambos and others, 2013 and in review). Dual-frequency GNSS data were recorded using an integrated Topcon GRS-1 receiver with a PGA-1 antenna. Data were recorded at 30 s intervals in multiple 20 min sessions each day (between 3 and 5 depending on power availability). Data were processed against publicly available Polenet stations on Thurston

Island, Bear Peninsula and Backer Island. Multiple base stations were necessary, because the record at any one of these stations is incomplete. All data were processed kinematically using the track processing module of MIT's GAMIT/GLOBK software (Herring and others, 2018). The resulting positions were converted to the Antarctic Polar Stereographic projection (EPSG:3031) using the transformer class from Python's pyproj library (Whitaker and others, 2019). They were then cleaned for obvious outliers (more than 3 m variation from a second order fit of time versus each coordinate) and transformed into an along-flow and cross-flow coordinate system. Finally, speeds were derived after smoothing the along-flow component with a lowess filter using the non-parametric package of Python's statsmodels library (Seabold and Perktold, 2010).

### 2.2.3 Distributed temperature sensing at Cavity Camp

Hot water drilling was undertaken at Cavity Camp on 30/31 December 2019. A distributed temperature sensing (DTS) fiber-optic cable was deployed with an ocean mooring to collect temperature profiles of the ice–ocean column with a 25 cm vertical resolution. The recording period spans from 2 January 2020 to 7 October 2021, with data collected every 4 h in summer for detailed monitoring and reduced to every 24 h or one per week during winter for power conservation. Calibration of the DTS record was conducted against two SeaBird MicroCAT SBE 37-IMPs measuring conductivity, temperature and depth installed in the ocean mooring at 520 and 744.5 m depth below the ocean surface. The calibration used a two-point slope and offset method (Dotto and others, 2022). Temporal gaps in the DTS data were either due to malfunctioning of the telemetry or low power. The DTS record is utilized to interpret the vertical strain profile derived from our ApRES record at Cavity Camp.

To ensure a consistent water supply for hot water drilling, a temporary water reservoir was created within the borehole, allowing water recirculation facilitated by a submersible pump and surface heaters. This reservoir, situated ~45 m below the surface, indicated pore close-off, preventing water loss into the permeable firn. Additionally, a brief delay occurred ~235 m during the second reaming of the borehole, suggesting potential enlargement of the hole at this depth and resulting in a second heat anomaly near the ice-shelf base.

### 2.3 Damage modeling

Damage in ice reflects the cumulative stress and melt history of the ice shelf. Damage primarily accumulates within an ice parcel when shearing and extension overcome the local gravitational driving force and cause microscopic voids or fractures to progressively grow over time (Bassis and Ma, 2015). When vertically integrated over a column of ice, damage ( $D$ ) signifies the fraction of the ice column through which fractures or crevasses extend ( $D=0$  indicates no damage,  $D=1$  indicates fully broken ice). Basal melt affects vertically integrated damage by either preferentially eroding healthy ice (e.g. Kachuck and others, 2020) or damaged ice (e.g. Bassis and Ma, 2015; Sun and others, 2017). Damage parameters have been shown to reproduce the calving lengths of ice tongues (Kachuck and others, 2022) and indicate rheological preconditioning of ice to weakness and failure (e.g. Borstad and others, 2016; Lhermitte and others, 2020).

To estimate the damage in the Thwaites Eastern Ice Shelf, we apply the pseudo-plastic, long-wavelength instability theory proposed by Bassis and Ma (2015). This theory identifies strain and stress conditions under which vertically integrated damage, expressed as a perturbation in the ice thickness, will either grow or shrink as the ice advects downstream and is subject to melt.

The evolution equation is as follows:

$$\frac{\partial D}{\partial t} + u \cdot \nabla D = \left[ n(1 - S_0)\epsilon_1 + \frac{m}{h} \right] D \quad (1)$$

where  $u$  is the ice velocity,  $n=3$  is the Glen flow law exponent,  $S_0$  is a dimensionless number representing the ratio between hydrostatic pressure and the largest principal deviatoric stress within the ice shelf,  $\epsilon_1$  is the largest principal strain rate,  $m$  is the melt rate (positive) both within and outside of the crevasse and  $h$  is the ice thickness (see Kachuck and others, 2020). The initial numerical perturbation is the Nye zero-stress crevasse depth, where hydrostatic pressure surpasses tensile stress. Assuming that the damage progresses from steady state in 2014 (by solving Eqn (1) with  $\partial D/\partial t=0$ ), we use Eqn (1) to compute the increment of damage at subsequent observation times solely based on measurements of surface velocity and ice thickness along flowlines to update each term in the equation (using a forward Euler step and an upwind derivative for advection).

Adopting a mass-conservation approach, we simulated the transient evolution of BedMachine ice thickness from an initial date of 2014 to the conclusion of the Sentinel-1 observational period in 2023. Advecting the thicknesses is crucial due to the considerable variability in ice thickness on the Thwaites Eastern Ice Shelf, ensuring the mitigation of the potential spurious effects of a mismatch between the observed velocities/strain-rates and local ice thickness. We formulate ice advection by solving the below equation:

$$\frac{\partial h}{\partial t} = m - u \frac{\partial h}{\partial x} - h\epsilon, \quad (2)$$

with an implicit numerical scheme. The damage model is confined within the bounds of the evolving ice thicknesses and does not extend beyond where ice thickness drops to zero.

We perform two experiments, one without basal melt, and one using the basal melt rate field from Adusumilli and others (2020) applied to the advecting ice thickness profile and the damage evolution equation. This approach allows us to distinguish between the impact of basal melting and ice-dynamical processes on the modeled damage by comparing results obtained with and without basal melting. The computed damage provides insights into periods in the Thwaites Eastern Ice Shelf's strain-rate history during which we anticipate damage accumulation, advection and ice weakening. It also identifies periods when damage would have been less likely to increase, or the ice would have partially healed.

## 3. Results

### 3.1 Rifting and calving

We monitored the development and subsequent progression of several sets of fractures on the Thwaites Eastern Ice Shelf. The first set comprises five distinct rifts that cross the central region of the ice shelf (Fig. 1c). These rifts originated in the shear zone upstream of the pinning point. In this zone, the nearby ice melange from the former Thwaites Western Glacier Tongue flows unimpeded into the ocean (Fig. 1). The rifts extend toward a large basal channel (Fig. 1a), which separates the highly fractured region near the grounding zone from the relatively intact central region of the Eastern Ice Shelf.

In January 2016, two large rifts emerged from the shear zone, marked as dark blue and pink rifts in Figure 1c/d, with initial lengths of ~1 km. They maintained this length for most of 2016 but experienced rapid growth to ~5 km near the end of the year. This austral spring/summer episodic growth recurred in

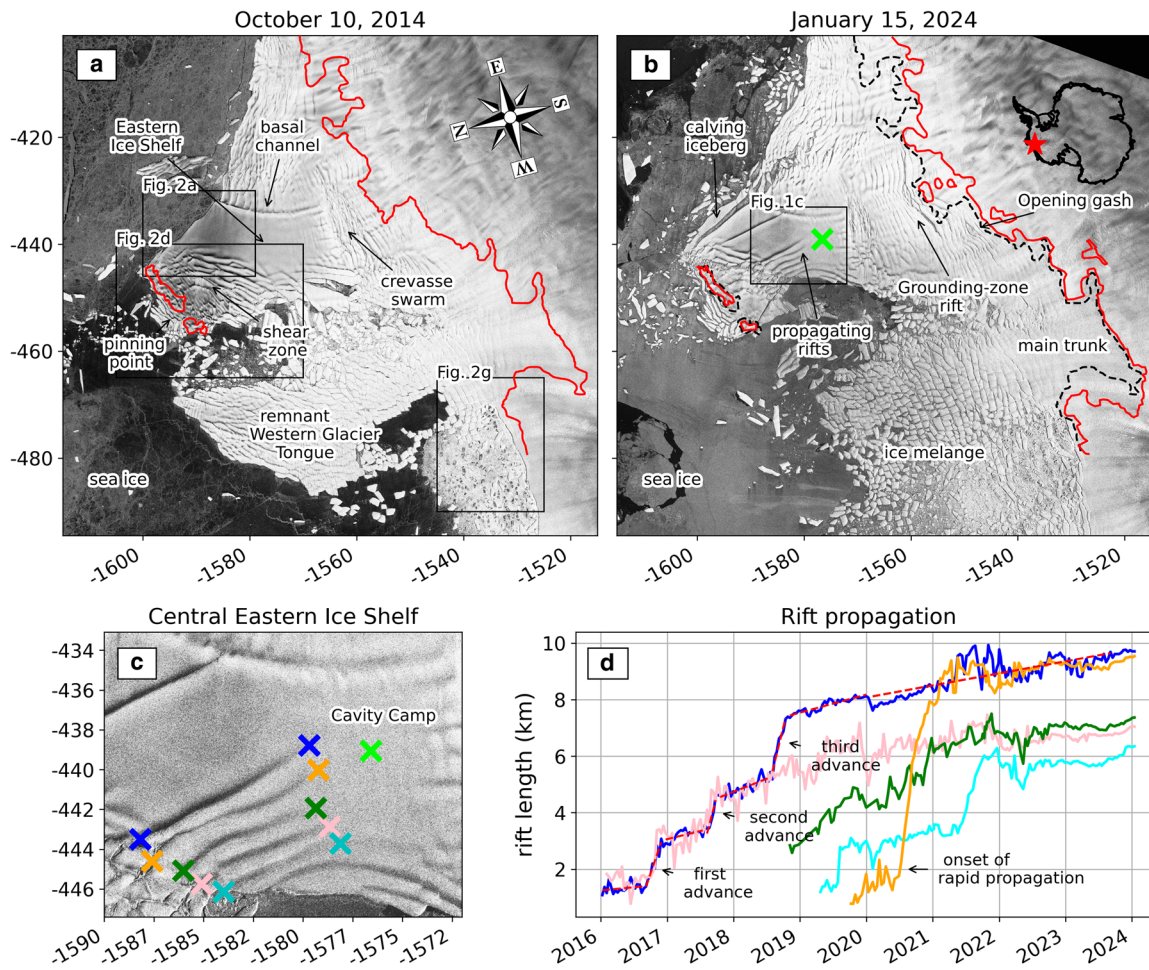


**Figure 1.** Rift development on the Thwaites Eastern Ice Shelf. (a) Sentinel-1a image captured in October 2014 displaying key features discussed in the main text. The red line corresponds to the 2014 grounding zone (Wild and others, 2021). The three black rectangles show the extents of Figure 2, focusing on the eastern calving front, the western calving front and a region near the main trunk of the Western Glacier Tongue. (b) Sentinel-1a image from January 2024 highlighting recent ice-dynamic processes discussed in the text. The black rectangle marks the region shown in panel (c). The green cross represents the location of Cavity Camp. Observe the retreat of the grounding zone and the reduction in pinning point area, as indicated by the 2020 grounding-zone product (Wild and others, 2021). The red star in panel (b) inset marks the location of the Thwaites Eastern Ice Shelf in the Amundsen Sea Embayment of West Antarctica. (c) Central ice-shelf area with colored crosses mark the starting and ending points of five rifts. (d) Time series of rift growth since January 2016, emphasizing distinct events in the latter half of the years when rifts lengthen episodically or emerge anew.

2017 for both rifts, but in 2018, it was only observed for the dark blue rift, which grew at a maximum rate of  $9.5 \text{ km a}^{-1}$ . Both the dark blue and pink rifts have maintained relatively slow and steady growth rates since the end of 2018. However, three new rifts have formed since that time. The green rift made its appearance at the end of 2018 and steadily grew at a rate of  $\sim 1.5 \text{ km a}^{-1}$ , without clear episodic events. The cyan rift emerged in mid-2019 and consistently grew through 2020, undergoing an expansion from  $\sim 3.5 \text{ km}$  in length to  $\sim 6 \text{ km}$  in mid-2021. Another rift (marked in orange) formed just upstream of the blue rift at the end of 2019. It grew with a steady rate of  $\sim 1 \text{ km a}^{-1}$  throughout 2020, but rapidly lengthened from  $\sim 2 \text{ km}$  to over  $8 \text{ km}$  in the austral summer of 2020/21. Once it reached the length of the dark blue rift, the orange rift continued to lengthen at a rate of  $\sim 0.5 \text{ km a}^{-1}$ . Since the beginning of 2022, all five rifts have been lengthening steadily without the occurrence of rapid events.

The Thwaites Eastern Ice Shelf, being laterally unconfined, generates tabular icebergs on both its eastern and western flanks. In March 2017, a complete-depth rift emerged on the eastern side, stretching  $\sim 16 \text{ km}$  from the eastern part of the pinning point to the basal channel (labeled feature I in Fig. 2b), parallel to the set of five rifts discussed above. A second rift emerged further downstream in September 2017 (feature II) leading to the separation of an  $\sim 18 \text{ km}$  long and  $2 \text{ km}$  narrow iceberg (feature III;

Benn and others, 2022; also Figs 1b, 2a–c). Intriguingly, this rift initiated at the mouth of the basal channel and spread across the ice-shelf front toward the pinning point within 1 month, implying different underlying processes compared to those driving the initial rift.

The eastern rift shown in Figure 2b (feature I) isolated a section of ice shelf that would form an iceberg of  $\sim 55 \text{ km}^2$  should the remaining connections calve along the basal channel. This calving style would be similar to the separation of the tabular iceberg in Figure 2c along the channel, and to other channel-influenced calving events observed on other ice shelves such as Pine Island (Alley and others, 2023), although it would create a considerably larger iceberg than previously observed on the Thwaites Eastern Ice Shelf. Apart from the 2017 calving event, the eastern side has primarily witnessed the release of relatively small icebergs. The western flank has been steadily eroded by the fast-moving ice melange draining through Thwaites Glacier’s main trunk. In 2023, two tabular icebergs,  $\sim 21$  and  $14 \text{ km}^2$  in size, calved into the former ice melange area (labeled features IV and V in Figs 2d–f). A third iceberg, measuring  $\sim 19 \text{ km}^2$ , remains loosely attached (at least as of 15 January 2024), but calving appears imminent, which would directly weaken the connection between the ice shelf and the western portion of the pinning point (feature VI in Fig. 2f).

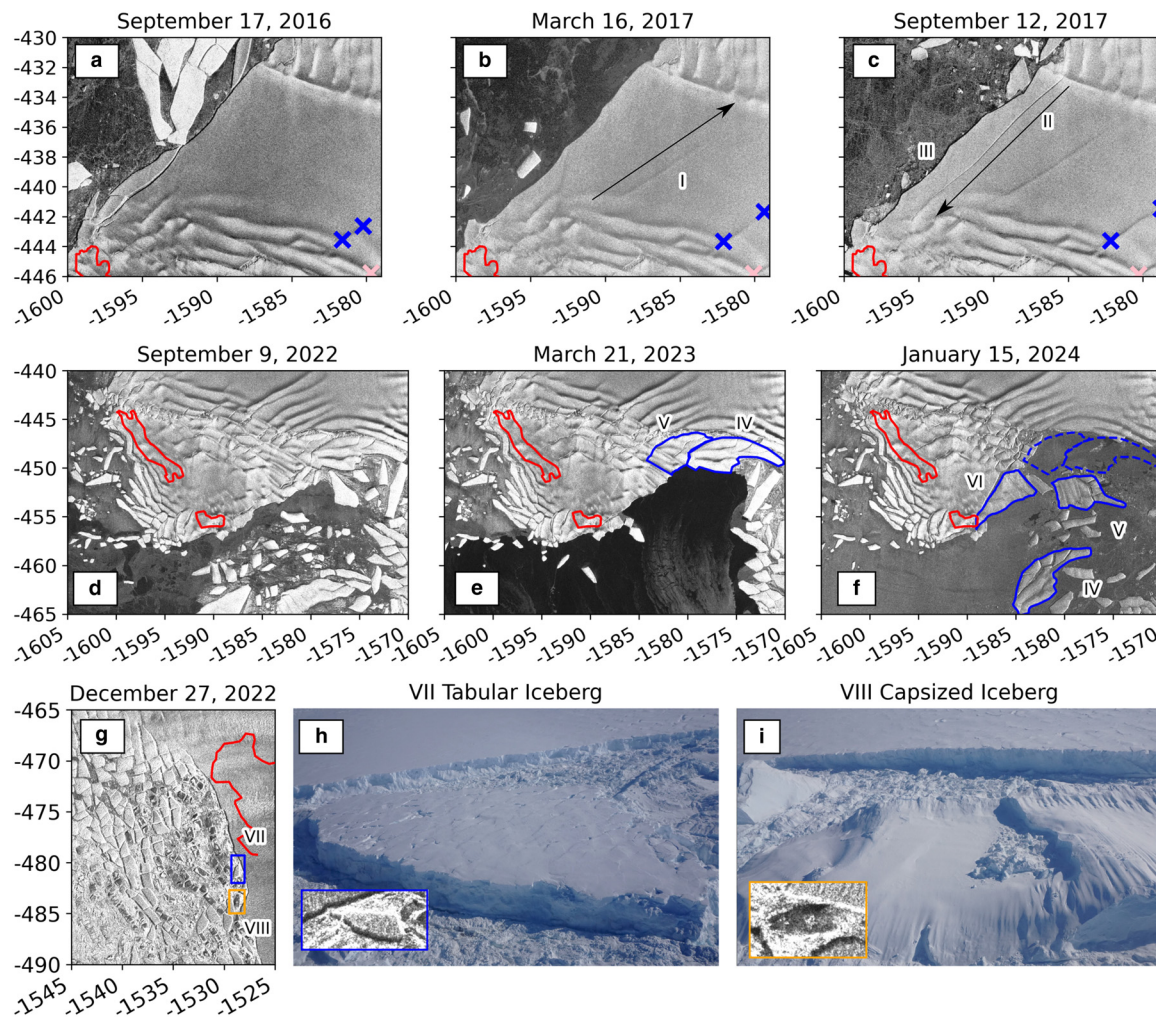


**Figure 2.** Recent ice-shelf calving events. See Figure 1 for the location of these three regions. (a–c) Eastern calving front. (a) An undamaged ice shelf with no observable rifts. (b) Rift formation extending from the pinning point across the central portion of the ice shelf toward the basal channel (feature I). (c) Subsequent rift development along the ice front from the basal channel to the pinning point (feature II), leading to the calving of a narrow iceberg in mid-2017 (feature III). (d–f) Western calving front. (d) The presence of a shear margin and ice melange confined by sea ice. (e) Disintegration of sea ice and the emergence of open ocean waters in the former shear margin. (f) Recent activation of the western calving front with the calving of two icebergs in mid-2023 (features IV and V) and an imminent calving event near the western section of the pinning point (feature VI). (g–i) Calving near the main trunk. (g) Bright and dark icebergs present in Sentinel-1a imagery. The blue and orange rectangles show the locations of photographs in panels (h) and (i). (h) An  $\sim 1.3$  km wide tabular iceberg with  $\sim 100$  m freeboard (feature VII). (i) An equally wide capsized iceberg revealing a submerged 600 m ice column displaying vertical fluting signatures as signs of past melt (feature VIII). Red lines in all panels correspond to the 2020 grounding-line product (Wild and others, 2021).

To the west of Thwaites' main trunk, the grounding zone has maintained a relatively stable position, anchored on a bathymetric ridge (Fig. 2g; Milillo and others, 2019; Wild and others, 2022). At this calving front, icebergs have continuously calved since the commencement of the Sentinel-1 record in 2014 (Supplementary video). This site is the only location along Thwaites Glacier's extensive grounding zone where icebergs capsize and become visible as dark patches shortly after detaching from the calving front (Fig. 2g). These calved icebergs appear dark in radar imagery, because the recently submerged ice cliff reflects the radar signal away from the transmitting antenna more strongly than a snow-covered surface, resulting in a darker appearance in the backscattered amplitude, compared with bright tabular icebergs (feature VII). Photographic evidence reveals past melt features on these darker surfaces, extending vertically up the ice cliff in channel-like formations (labeled feature VIII in Fig. 2i).

### 3.2 Glacial strain rates and limited basal melt

We conducted ApRES measurements over a mean period of  $\sim 12$  d, covering 46 sites from December 2019 to January 2020 (Fig. 3a and

Tables S1/S2). Ice predominantly thins across the surveyed area, while a cluster of sites within the basal channel thickens (Fig. 3b). The median net thinning rates are  $1.07 \text{ m a}^{-1}$ , with a std dev. of  $1.02 \text{ m a}^{-1}$ , reaching  $3.78 \text{ m a}^{-1}$  at site 06. Median net thickening rates are  $1.56 \text{ m a}^{-1}$ , with a std dev. of  $0.81 \text{ m a}^{-1}$ , peaking at  $2.43 \text{ m a}^{-1}$  at site 31Up.

From the ApRES measurements, we can separate the derived rates of ice-thickness change into contributions from melt and ice dynamics (Section 2.2.1). The basal melt rates exhibit considerable spatial variability (Fig. 3c), ranging from  $-0.24 \pm 0.04 \text{ m a}^{-1}$  (indicating modest basal refreezing) near site 31 within the channel, to  $4.45 \pm 0.07 \text{ m a}^{-1}$  (indicating elevated localized melting) at site 06. In the study area, the median basal melt rate is  $0.88 \text{ m a}^{-1}$  with an average error of  $\pm 0.05 \text{ m a}^{-1}$ , as determined by the quality of the linear fit to the deformation of internal layers at each site (Section 2.2.1). Notably, both relatively high and relatively low basal melt rates coexist throughout the entire ice-shelf region, but none of these rates are very large in the context of ice shelves in West Antarctica (Adusumilli and others, 2020).

Net ice-thickness change depends on the relative magnitudes and signs of the basal melt/accretion rates and positive/negative

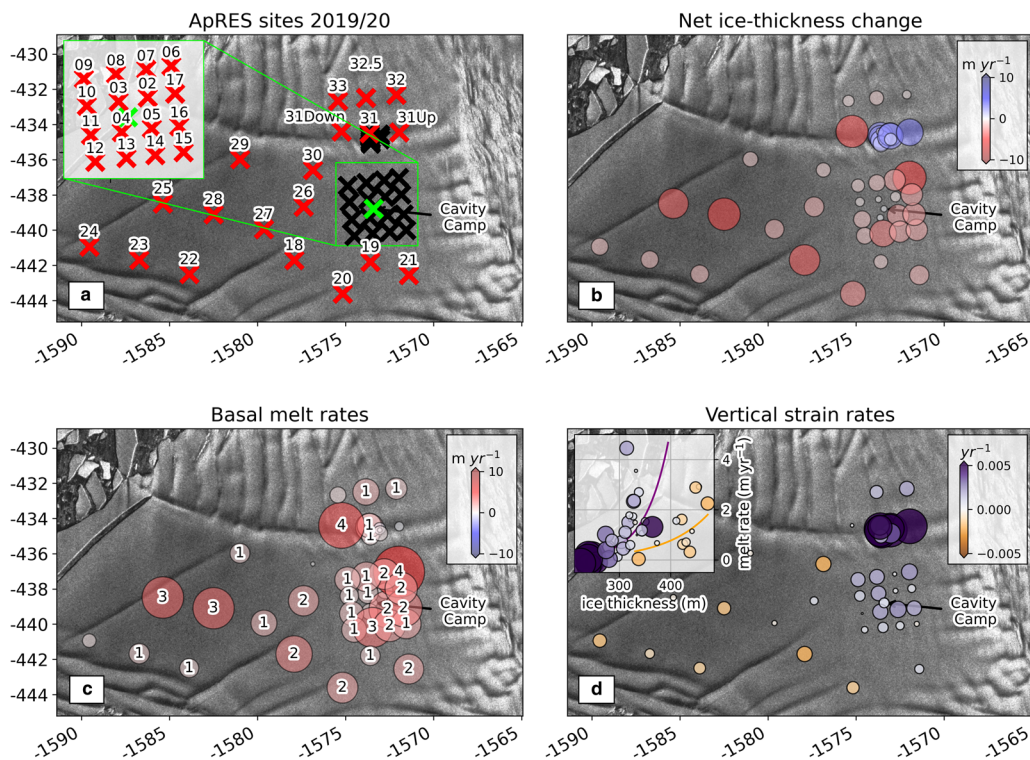


**Figure 3.** Spatial variability. (a) Sites on the Thwaites Eastern Ice Shelf measured using ApRES repeat-visits from December 2019 to January 2020. (b) Rates of net ice-thickness change during this period. (c) Basal melt rates as determined from ApRES measurements. Numbers show melt rates at sites over  $1 \text{ m a}^{-1}$ , circle size and color are proportional to the basal melt rate. (d) Vertical strain rates over the entire ice column. The inset shows the relationship between the local ice thickness, the determined melt rate and strain rate, with color-coded data points according to vertical strain rate magnitude and sign and best polynomial-fit curves for positive (purple) and negative (yellow) vertical strain rates.

strain rates. Specifically, an ice column with a positive strain rate will thicken if there is no basal melt. However, relatively large basal melt rates can remove ice more rapidly than is added through ice dynamics, causing the overall thinning of the ice column. We observe strain thickening at all sites surrounding Cavity Camp and a second cluster of sites in the channel area, reaching strain thickening rates of  $10.18 \times 10^{-3} \text{ a}^{-1}$ . The median positive strain rates measure  $1.85 \pm 0.38 \times 10^{-3} \text{ a}^{-1}$ . At the Cavity Camp site, the entire ice column dynamically thickens at a rate of  $0.83 \pm 0.26 \times 10^{-3} \text{ a}^{-1}$ . Given a local ice thickness of 297.14 m, the ice column thickens  $\sim 0.24 \pm 0.08 \text{ m a}^{-1}$ . Negative strain rates indicate dynamic thinning of the ice column, primarily due to horizontal extension of the ice shelf. Strain thinning is observed throughout the central region of the ice shelf downstream of Cavity Camp, particularly near sites of active rifting, with a median of  $0.97 \times 10^{-3} \text{ a}^{-1}$  and an average error of  $0.21 \times 10^{-3} \text{ a}^{-1}$ .

The inset in Figure 3d relates ice thickness and melt rate, with the data divided into two populations: the sites with negative vertical strain, observed in the outer regions of the ice shelf, are shown in orange shades, while the sites with positive vertical strain, found in the inner regions of the ice shelf, are shown in purple shades. We observe that these two populations of vertical strain rates have some correlation with ice thickness, with generally thicker ice ( $\sim 400 \text{ m}$ ) experiencing strain thinning, and thinner ice ( $\sim 300 \text{ m}$ ) experiencing strain thickening (inset in Fig. 3d). We also observe a positive relationship between ice thickness and basal melt rate, and have fit an exponential curve to this relationship within both strain rate populations in the inset. This illustrates a difference in the degree of dependency of melt rate on ice thickness. Sites experiencing dynamic thickening reveal a stronger dependency of melt rates on ice thickness than sites that are experiencing thinning.

At Cavity Camp, we collected two types of measurements: continuous ApRES measurements and revisit measurements with a 22 d separation. The continuous ApRES data yielded a mean melt rate of  $0.13 \pm 0.01 \text{ m a}^{-1}$ , while the revisit measurements indicated a melt rate of  $0.11 \pm 0.04 \text{ m a}^{-1}$ . Both methods independently show relatively low basal melt rates. In Section 2.2.1, we use the continuous ApRES data to evaluate how representative the 22 d separation is, finding that a 3 d interval would have been sufficient to capture a reliable melt rate at Cavity Camp. With our 46 sites across the ice shelf having an average measurement interval of 12 d (ranging from 6 to 23 d), we are confident that these sites are representative. The mean basal melt rate over 274 d of continuous ApRES data at Cavity Camp is  $0.13 \text{ m a}^{-1}$ , and exhibits a substantial temporal std dev. of  $0.6 \text{ m a}^{-1}$  (Fig. 4b). We applied a Chebyshev low-pass filter with a 7 d cutoff frequency to smooth the melt rate data to weekly values (Fig. 4b). The smoothed record reveals a reduced std dev. of  $0.12 \text{ m a}^{-1}$  over time. Neither discernible seasonality nor a significant trend in basal melting was detected, although we note that the observational record is limited to the first 8 months of the year, limiting our ability to evaluate seasonality. Toward the end of the record, basal melt rates appeared to rise, accompanied by considerable temporal fluctuations. The observed temporal fluctuations are closely linked to the 14 d spring–neap tidal cycle (Fig. 4a).

We conducted a continuous wavelet analysis on the data, revealing significant variations in the diurnal and semi-diurnal tidal bands for both basal melting and strain deformation (Figs 4c, e). The power fluctuations in both records exhibit modulations, which initially correspond to a fortnightly spring–neap tidal cycle in 2020 (yellow regions within black contours in Figs 4c, e). Following re-installation of the ApRES in January 2022, the basal melt rate retained these fortnightly variations, while

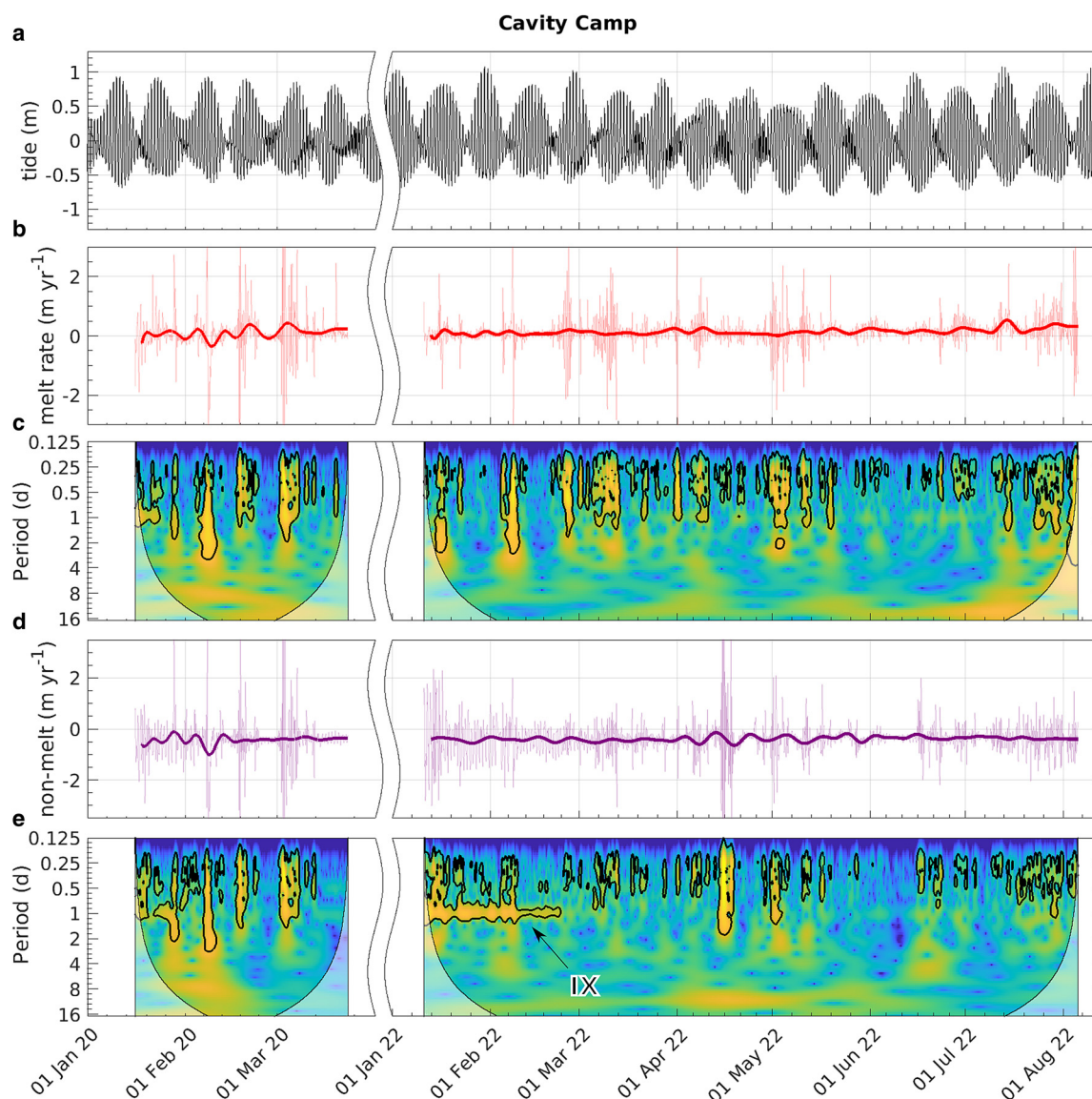


**Figure 4.** Tide and melt temporal co-variability at Cavity Camp. (a) Tidal heights based on the CATS2008 model (Howard and others, 2019, an updated version of the model by Padman and others, 2002), reflecting a 14 d spring-neap tidal cycle. (b) and (d) Time series of ApRES-derived basal melt rate and the non-melt signal representing vertical strain deformation near the ice base. The 3 hourly time series are shown, along with weekly filtered means. (c) and (e) Continuous wavelet power spectra of the normalized melt rate and strain rate records to identify periodic patterns across different timescales. Warm colors indicate high power, cold colors indicate low power within a certain temporal band. Black contours designate the 5% significance level against noise to identify localized intermittent periodicities. The cone of influence, where discontinuities at the edges might distort the continuous wavelet transform, is shown as a lighter shade. Note feature IX that marks the time when diurnal signals in the non-melt time series diminish. There is a period with no data, represented by the wave mask in all panels.

the non-melt signal gradually lost its diurnal component until March 2022 (feature IX). Over the 2 years between the initial ApRES deployment in January 2020 and the re-installation visit in January 2022, Cavity Camp migrated  $\sim 1.5$  km with the ice flow. During this migration, Cavity Camp might have transitioned from a compressional regime to a gradient-weak ice-dynamic region, where ‘gradient-weak’ refers to an area with a relatively small spatial variation in ice velocity and strain rates.

The continuous record at Cavity Camp also allowed us to evaluate the long-term vertical pattern of strain within the ice column. We conducted cumulative displacement calculations for 20 m depth bins for the first 80 d of the 2022 record, before noise briefly disrupted the dataset (we note, however, that the characteristic vertical strain profile remains consistent through the second half of the 2022 record). From this data subset, we only considered data below a 50 m firn layer and above 280 m to avoid any spectral leakage from the basal return (Fig. 5a). The resulting vertical strain profile displays a distinct shape, resembling a question

mark with respect to depth (Fig. 5b). Between the depths of 50 and 100 m, the ice exhibited rapid thickening at  $8.99 \times 10^{-3} \text{ a}^{-1}$ , or  $\sim 2 \text{ m a}^{-1}$ , corresponding to 4% strain during the observational period. Below this layer of rapid thickening, the ice column transitions to substantial thinning at  $12.33 \times 10^{-3} \text{ a}^{-1}$  between 130 and 180 m, or  $\sim -2.8 \text{ m a}^{-1}$ , corresponding to  $-6\%$  strain during the observational period. Beneath 180 m, the vertical strain followed a nearly linear trend of  $-0.11 \times 10^{-3} \text{ a}^{-1}$ , indicating slow thinning due to horizontal extension near the ice base.

We used the linear section of the vertical strain profile near the base of the ice column to predict the thickness of an ice shelf primarily undergoing strain-induced deformation (Fig. 5b). The results revealed ice-shelf thinning attributed to strain deformation at  $0.42 \pm 0.01 \text{ m a}^{-1}$ . Over the 80 d period of this data subset, the measured local ice thickness decreased by 0.11 m from its initial value of 299.56 m, as determined from the peak reflection in the continuous ApRES data. Extrapolating this from 80 d to a 1 year period, we observe an absolute ice thickness change of



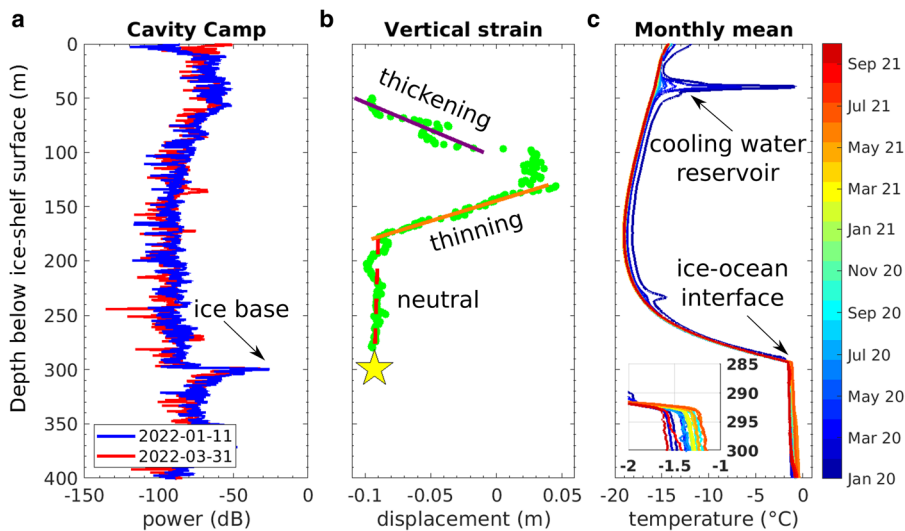


**Figure 5.** Question-mark-shaped vertical strain profile at Cavity Camp. (a) Initial and final ApRES trace over an 80 d period in early 2022. The peak  $\sim 300$  m marks the ice base location. (b) Cumulative displacement of coherent internal reflectors during this time, with a rapid increase in vertical displacement denoting thickening in the upper half of the ice column (purple line), followed by a sharp decrease indicating subsequent thinning between 130 and 180 m depth (orange line). The dashed red line represents the linear fit of a depth range depicting the integrated vertical strain in the lower ice column. The location of the yellow star indicates the vertical displacement of a non-melt deforming ice base. (c) Vertical temperature profiles from the DTS averaged monthly.

$-0.51 \text{ m a}^{-1}$ , with  $-0.42 \pm 0.01 \text{ m a}^{-1}$  attributed to strain-induced effects (82%), leaving  $\sim 0.09 \pm 0.01 \text{ m a}^{-1}$  as the estimated basal melt rate and error estimate. This agrees well with the short-term melt rate estimate of  $0.11 \pm 0.04 \text{ m a}^{-1}$  derived from the 22 d repeat-visit survey from December 2019 to January 2020. This melt rate is also consistent with the long-term melt rate of  $0.13 \pm 0.01 \text{ m a}^{-1}$  calculated from the complete continuous ApRES dataset at Cavity Camp.

The temperature profile within the borehole beneath Cavity Camp exhibits characteristics typical of an ice shelf experiencing basal melting (Fig. 5c). The profile starts at  $\sim -15^\circ\text{C}$  at the ice surface, gradually decreasing to  $\sim -19^\circ\text{C}$  at a depth of 170 m, followed by a sharp increase in temperatures toward the pressure melting point at the ice–ocean interface. The cold ice core of the shelf is a result of advection of ice that originates from higher up on the ice sheet where the snow was deposited at lower temperatures. The residual heat from the initial hot water drilling diminishes rapidly within the initial months (Figs 5c, d), evident particularly  $\sim 45$  m depth in the cooling water reservoir. After the initial cooling period, the temperature profile reflects long-term averages. Notably, the depth of the ice–ocean interface remains constant at 292 m throughout the 21 month duration (Fig. 5c), indicating weak local melting, which agrees with the ApRES observations at Cavity Camp (Fig. 3c and Dotto and others, 2022).

### 3.3 Ice-flow acceleration

We depict our velocity record using Hovmöller diagrams, evaluating ice speed and longitudinal strain changes along three flowlines (dashed lines in Figs 6a, b). These flowlines all originate from the grounded section of Thwaites Glacier, traverse its grounding zone onto the floating ice shelf, and exhibit distinctive features. The eastern flowline (light blue) traverses a series of grounding-line rumpled identified from height above flotation (Wild and others, 2022) and a recent rift, and then approximately follows the basal channel to reach the eastern calving front. The central flowline (green) crosses the grounding-zone rift, the crevasse swarm originating from the 2005 peak in flow speed, Cavity Camp, and the site of the 2017 iceberg calving event. The western flowline (orange) passes through a newly opened grounding-zone gash, follows the shear zone toward the pinning point, and concludes just upstream of the pinning point's eastern section.

Figure 7 illustrates the evolution of ice speed and longitudinal strain along the eastern (light blue) flowline along the basal

channel since the launch of Sentinel-1 in 2014. The transect intersects the grounding zone at  $\sim 127$  km, denoted by the rapid transition from slower to faster speeds (cooler to warmer colors, respectively). While the grounded section primarily flows at speeds below  $1.0 \text{ m d}^{-1}$  (or  $350 \text{ m a}^{-1}$ ) throughout the record, the floating portion experienced a significant acceleration starting  $\sim 2020$ , reaching over  $2.5 \text{ m d}^{-1}$  (or  $>900 \text{ m a}^{-1}$ ) by mid-2023 (Fig. 7b). The floating ice has accelerated between 70 and 90% since 2020. Acceleration is also present just upstream of the grounding zone (116–127 km along the transect), but by 20–25%, a much smaller magnitude than on the floating portion. The speed record also reveals sharp gradients, leading to distinct bands of localized extension in the longitudinal strain rate record (Fig. 7c). The most noticeable of these bands is located at the grounding zone and starts to move downstream in 2021. This suggests that the grounding-zone position at this site was stable before this movement occurred. Localized strain is also observed as a number of bands further upstream of the grounding zone. Offshore, toward the eastern edge of the ice shelf, an even more pronounced kinked extensional band emerged in 2017, signifying the calving of the narrow iceberg at the eastern front (Figs 2a–c). Between this region and the grounding zone, ice speed displays weak gradients, tending toward slight longitudinal compression along the basal channel. These observations align with a relatively uniform level of modeled damage along the basal channel (Fig. 7d), especially in the vicinity of the crevasse swarm  $\sim 140$  km. However, there is a notable increase in damage during 2019 coinciding with a temporary retreat of the grounding zone. Ice parcels in this area, exhibiting heightened damage, underwent further evolution without substantial dissipation and eventually advected to the location where the grounding-line rift is initially observed in 2022 (feature X).

Figure 8 illustrates ice-dynamic processes along the central flowline, which traverses Cavity Camp in the central section of the ice shelf. The grounding-zone position retreated between 2017 and 2018, and acceleration notably intensified in 2020, when a swift ice-shelf-wide acceleration took place (Fig. 8b). Mirroring the trends observed along the eastern (light blue) flowline, this acceleration ranges between 70 and 90% for floating ice and 15 and 20% for grounded ice since 2020. Additionally, the 2017 calving event on the eastern flank is evident, displaying the downstream drift of the iceberg. Slightly downstream of the grounding zone, a narrow zone of longitudinal extension abruptly narrowed and intensified in early 2021 (Fig. 8c). This marks the creation of a lengthy rift (feature XII), parallel to the grounding zone, extending for over 15 km (Fig. 6c). This substantial

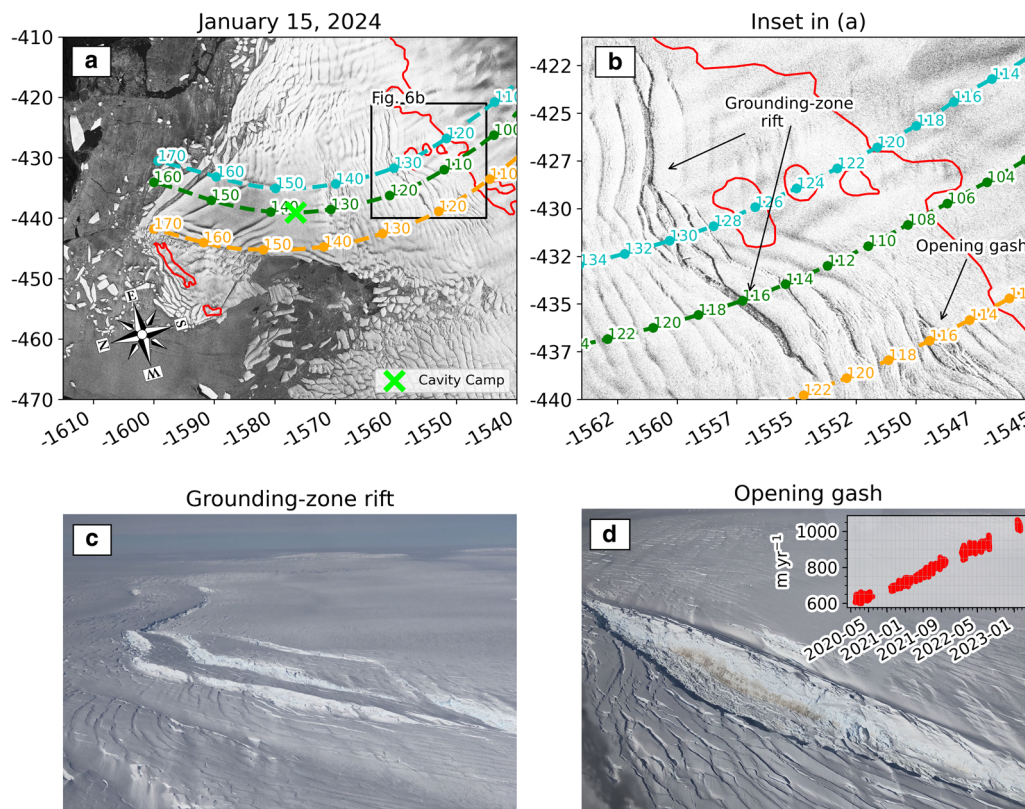


**Figure 6.** Grounding-zone rift evolution. (a) Ice-flow lines across the Thwaites Eastern Ice Shelf, including the basal channel, central zone through Cavity Camp and the shear zone, are represented in Hovmöller diagrams showing the flow acceleration. The eastern flowline (light blue) is depicted in Figure 7, the central flowline (green) is shown in Figure 8 and the western flowline (orange) is illustrated in Figure 9. Numbers show distance in km along the flowlines. (b) Close-up of the central area with the recently formed grounding-zone rift and an opening gash. (c) and (d) January 2022 photos of these features. The inset in panel (d) presents the acceleration of ice-flow speed measured with a GPS at Cavity Camp since January 2020.

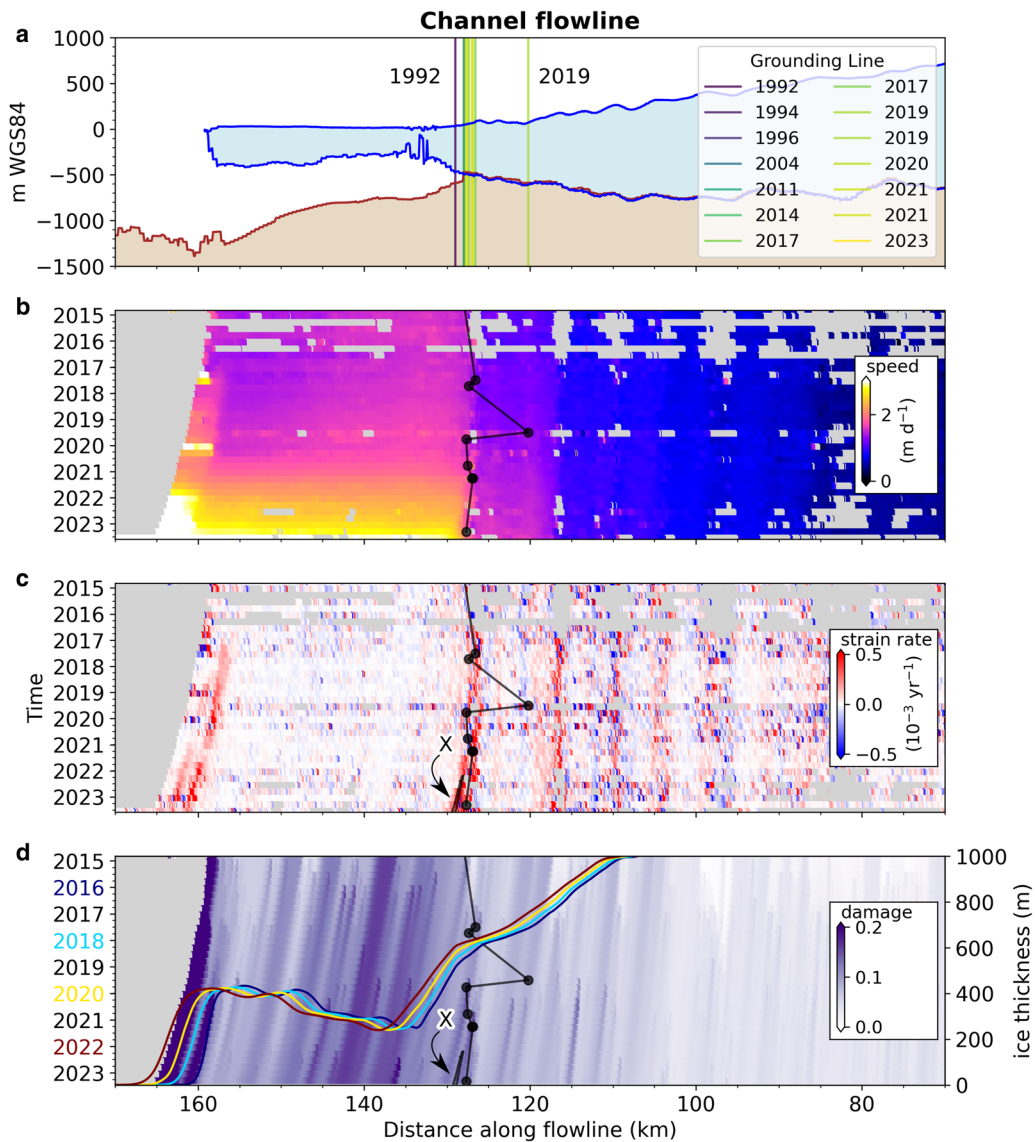
extensional zone advanced at the speed of ice-shelf flow, moving  $\sim 3$  km downstream by the end of our record in mid-2023. In the central region, where the flowline crosses the crevasse swarm and the vicinity of Cavity Camp (feature XIII), there are indications of slight compressional strain rates. Over time, the initially narrow band of damage at the crevasse swarm widens (feature XV) as the ice-thickness minimum spreads over a large area during downstream advection. Localized damage increases in 2016, coinciding with the grounding-zone retreat, yet lacks discernible surface crevassing in satellite observations. In 2021, the feature XII reappears at  $\sim 115$  km along the flowline, aligning with visible surface crevassing (identified as the grounding-zone rift in our analysis). Another noticeable feature of increased damage at 132 km in 2019 is an artifact of the data, attributable to a missing observation at that specific time and location (features XI and XIV).

Figure 9 evaluates changes along the western (orange) flowline that crossed the gash (Fig. 6a). The acceleration of the Thwaites Eastern Ice Shelf is particularly conspicuous along this flowline, ranging from 60 to 125% relative to the 2020 levels. Grounded ice exhibited a modest acceleration of 15%. The flowline terminates just east of the pinning point. Notably, the Hovmöller diagram illustrates a zone of longitudinal compression between  $\sim 150$  and 160 km (Fig. 9c), likely attributable to backstress transmitted by the pinning point. Further upstream, at the grounding-zone location, bands of extensional stresses remained relatively stable, indicating a consistently positioned grounding zone throughout the record. In early 2021, a narrow band of extension nucleated just downstream of the grounding zone and quickly advanced  $\sim 3$  km onto the floating part of the ice shelf (feature XVI). At this location, we observed the rapid opening of a gash (Fig. 6d). The gash extended through the entire thickness of the ice, as

indicated by the visible sediments adhering to the base of the newly exposed cliff face. Unlike tabular icebergs, the cliff face rolled over as the gash opened, revealing the section of the ice cliff that had been submerged. This iceberg overturning is similar to behavior observed further west along Thwaites Glacier's grounding zone, where calving icebergs tend to capsize (Figs 2g–i). The damage model results reveal the accumulation of damage prior to the initiation of the gash in 2019, persisting until its eventual opening in 2021 (feature XVI in Figs 9c, d). Additionally, a distinct feature is observed as an evident surge in damage terminating at  $\sim 160$  km, corresponding to the flowline's proximity to the pinning point. This specific region exhibits a gradual escalation in damage over time, underscoring the continuous impact on the ice shelf as it approaches the pinning point and weakening of the shear zone.

### 3.4 Fracture widening accounting for ice-flow acceleration

The Hovmöller diagrams in Figures 7–9 show considerable acceleration, particularly on the floating ice shelf, and they also demonstrate that the highest strain rates are found along narrow features. This strain localization sometimes is observed along features that are persistent throughout the entire record, such as the grounding zone or at locations above the grounding zone that might be controlled by subglacial topography. In other cases, strain can be concentrated in fractures, many of which change significantly during the observational period. The Cavity Camp flowline (Fig. 8) provides a unique opportunity to investigate patterns of strain distribution in an accelerating and fracturing ice shelf.



**Figure 7.** Eastern (light blue) flowline along the basal channel. (a) Inferred ice geometry along the flowline as derived from the reference elevation model of Antarctica (REMA; Howat and others, 2019) and BedMachine Antarctica Version 3 (Morlighem and others, 2020; Morlighem, 2022) data. Ice is represented in blue, while bed is depicted in brown. Vertical lines mark grounding-line locations. Hovmöller diagrams depict (b) flow speed and (c) longitudinal strain rate. Each row on the diagram represents the magnitude of the variable (color) with respect to distance along the flowline; each column is how that location changes from year to year. The black line in panels (b)–(d) corresponds to the location of the grounding zone. The black line where the arrow is pointing to in panel (c) corresponds to our along-flow picks of the grounding-line rift in Sentinel-1 imagery (feature X). (d) Hovmöller diagram for modeled damage (purple shades) superimposed with advected ice thicknesses along the flowline (scale on the right-hand y-axis) at the four times colored by corresponding year on the left.

The Cavity Camp GPS, which lies on the Cavity Camp flowline, operated from early 2020 through mid-2022. At the time of installation, the GPS was moving at a rate of  $\sim 1.65 \text{ m d}^{-1}$ , but it experienced an acceleration of  $\sim 70\%$  by the end of the record. We calculated the cumulative distance that this GPS moved during this observational period. We also estimated the displacement that the Cavity Camp GPS would have experienced had the ice-shelf speed remained at a constant  $1.65 \text{ m d}^{-1}$ . The difference between these two trajectories – the observed trajectory with acceleration, and the estimated trajectory without – represents the excess displacement due to ice-shelf acceleration, and is plotted as a black line in Figure 10a.

Figure 8c shows an emerging area of strain localization due to the opening of a large rift (feature XII), which crosses the Cavity Camp flowline, starting in early 2021. We tracked the along-flow width of this rift, and plotted it as the blue line in Figure 10a. The dashed red lines represent polynomial fits to the observed GPS positions and the rift width. By comparing the excess GPS

displacement due to ice-shelf acceleration (feature XIII) and the width of the rift, we see that 100% of the excess displacement of the Cavity Camp GPS was accounted for by rift opening in April 2021 (Fig. 10b). As time went on, the rift continued to open, but at a slower rate than the excess displacement experienced by the Cavity Camp GPS. During this time, the ice-shelf acceleration along the Cavity Camp flowline was accounted for in part by the continued rift opening, with the rest accounted for either by extension of other fractures or distributed extensional strain within the ice shelf that ultimately led to the accumulation of damage.

To the west along the grounding zone, we also monitored the widening of the gash, expanding both along-flow and across-flow. Its across-flow width, parallel to the grounding zone, is approximately ten times larger than its along-flow extension. The gash started opening in April 2021 with a width of 100 m, similar to the grounding-zone rift, and rapidly expanded to  $\sim 5 \text{ km}$  by mid-2022 in the across-flow direction. In the along-flow direction,

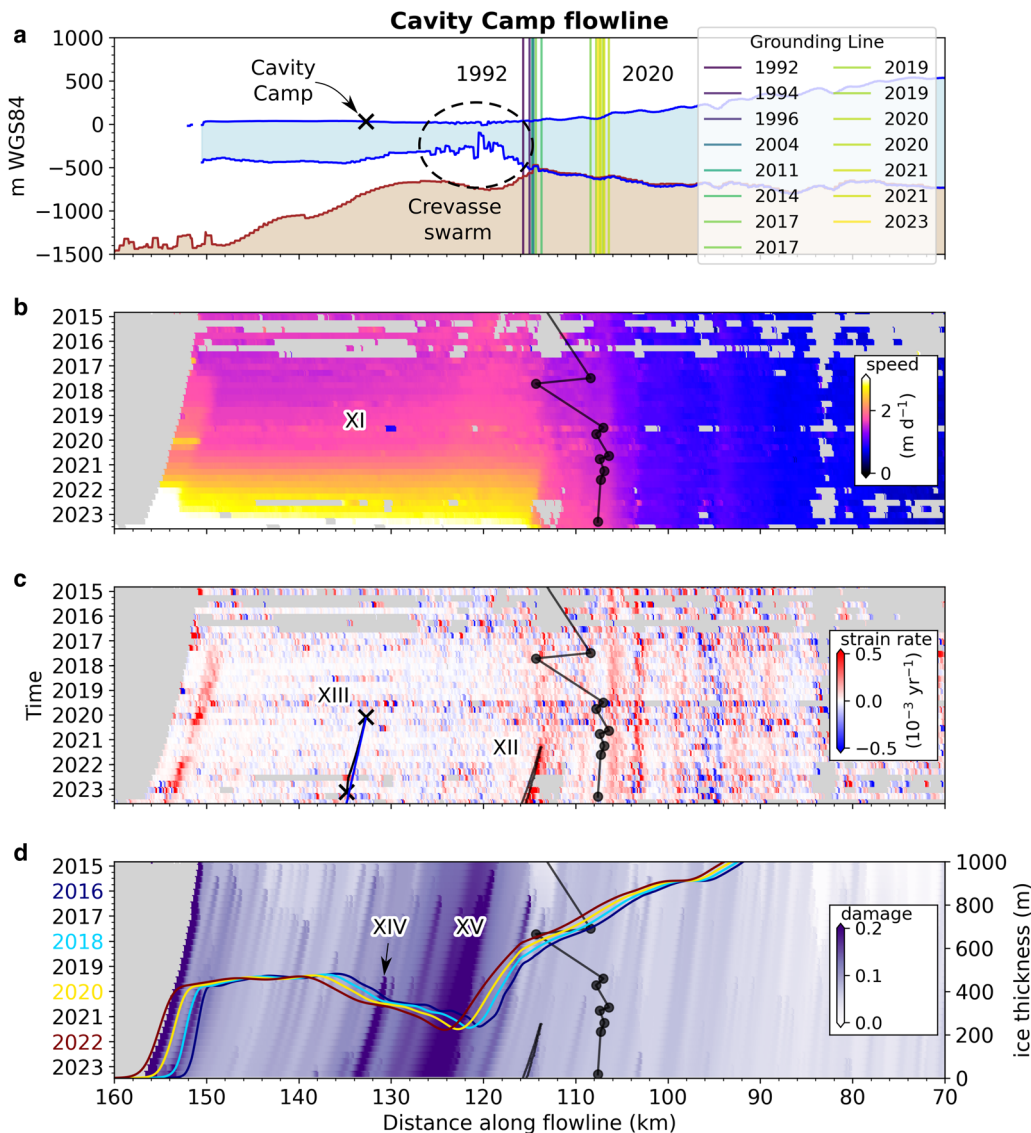


**Figure 8.** Central (green) flowline across Cavity Camp. (a) Inferred ice geometry along the flowline is derived from REMA and BedMachine data. Ice is represented in blue, while bed topography is depicted in brown. Vertical lines mark grounding-line locations. Hovmöller diagrams depict (b) flow speed and (c) longitudinal strain rate, with warm colors representing increased flow speed and extension, respectively. The black line in panels (b)–(d) corresponds to the location of the grounding zone. The feature XI shows the location of a data gap that triggered a spurious band of enhanced damage (feature XIV). The black line in panel (c) corresponds to our along-flow picks of the grounding-line rift in Sentinel-1 imagery (feature XII) as well as the location of Cavity Camp from GPS data (feature XIII). (d) Modeled damage and advected ice thickness along the flowline as described in Figure 7.

the gash width initially correlated with the ice-shelf acceleration downstream, as indicated by our velocity records, and continues to open steadily. This suggests that the localized strain observed along the grounding zone is also responsible for the gash opening. The increased localized strain at the grounding zone weakens the ice structure, making it more susceptible to fracturing. As the strain continues to concentrate in this area, it propagates downstream, contributing to the overall acceleration and the steady widening of the gash.

#### 4. Discussion

From the observations described in the previous section, we propose the following scenario for the evolution of the Thwaites Eastern Ice Shelf: initially, it underwent thinning primarily due to basal melt. As this thinning progressed, the shelf became less exposed to the deeper, warmer ocean waters, and a strong but thin stratification of the water column formed beneath the ice. This reduced basal melting, but the ice-shelf thinning

compromised the structural integrity of the ice shelf. Both rifting and shearing became significant, ultimately leading to fragmentation and (soon) disintegration (Benn and others, 2022). What distinguishes our narrative is the availability of observational data that allows for the precise differentiation between overall ice-column thinning and the individual contributions of melting and dynamic processes. The detailed and complex history obtained from the satellite record reveals the ways in which the ice shelf has helped stabilize Thwaites Glacier. Based on observations of the ice-shelf grounding zone and nearby coastline, we argue that the Thwaites Eastern Ice Shelf reinforces the stability of the grounding zone by preventing the capsizing of icebergs, and that we are likely to see a shift in this calving regime when the ice shelf is lost.

##### 4.1 Thwaites Ice Shelf basal melting regime

Ice-shelf thinning and weakening in West Antarctica due to basal melt has been widely documented over the satellite record (e.g.

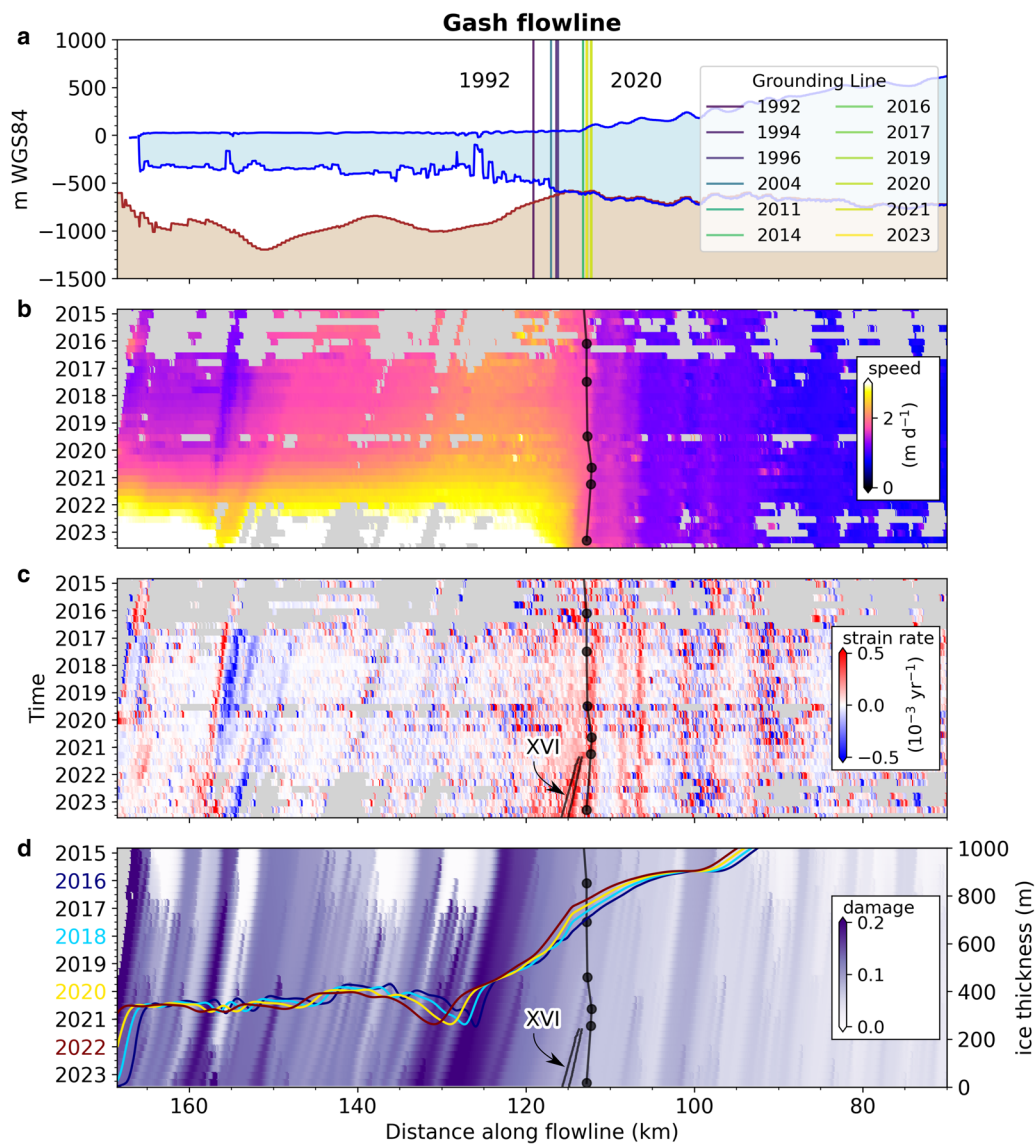


**Figure 9.** Western (orange) flowline across the opening gash. (a) Inferred ice geometry along the flowline is derived from REMA and BedMachine data. Ice is represented in blue, while bed topography is depicted in brown. Vertical lines mark grounding-line locations. Homöller diagrams depict (b) flow speed and (c) longitudinal strain rate, with warm colors representing increased flow speed and extension, respectively. The black line in panels (b)–(d) corresponds to the location of the grounding zone. The black line in panel (c) corresponds to our along-flow picks of the opening gash in Sentinel-1 imagery. (d) Modeled damage and advected ice thickness along the flowline.

Shepherd and others, 2004; Pritchard and others, 2012; Adusumilli and others, 2020). This enhanced forcing may have begun in the 1940s (e.g. Steig and others, 2013; Hillenbrand and others, 2017; Smith and others, 2017), causing sustained change in the Amundsen Sea. Multiple pathways of warm water intrusion influence the Thwaites Eastern Ice Shelf (Wählin and others, 2021), which have caused high melt rates, particularly in the area around the pinning point at the ice shelf's seaward edge. Satellite measurements suggest that thinning rates, largely driven by basal melt, may have modestly slowed overall beneath Thwaites between 1994 and 2012 (Paolo and others, 2015), and calculations of basal melt show a steady melt or a slight reduction (within error ranges) in the 2010–18 period compared to the 1994–2018 average (Adusumilli and others, 2020). However, calculated basal melt rates at Thwaites still show an excess of basal melt compared to that required to maintain a steady-state ice-shelf volume (Adusumilli and others, 2020), so basal melting still contributes to the disintegration of the Thwaites Eastern Ice Shelf.

Our repeat ApRES measurements support observations of temporally steady basal melt rates across the Eastern Ice Shelf,

but suggest that melt rates are spatially variable. The remotely sensed 24 year basal melt record provided by Adusumilli and others (2020) suggests a mean value of  $1.05 \text{ m a}^{-1}$  of basal melt on the Eastern Ice Shelf. Among 46 sites, we found a similar mean value of  $1.11 \text{ m a}^{-1}$  in our in situ data. However, std devs. differ significantly, with  $0.71 \text{ m a}^{-1}$  for Adusumilli and  $1.03 \text{ m a}^{-1}$  for our in situ measurements. Our larger std dev., relative to the mean melt rate, indicates small-scale heterogeneity in the melting process, not captured in smoothed and averaged satellite-derived basal melt rates. Differences between remote-sensing and in situ data are spatially clustered, with remote sensing tending to underestimate basal melt rates, especially at sites surrounding Cavity Camp, in the inner region where ApRES measurements reveal ice-column thickening. Remote estimation of basal melt rates involves satellite measurements of ice-shelf surface elevation changes and dynamic ice-thickness change. The use of a 24 year velocity mean for dynamic ice-thickness corrections in remote sensing may contribute to these differences, particularly in this most dynamic part of West Antarctica. Updating to more recent ice-divergence fields, as shown by Zeising and others (2022) on the

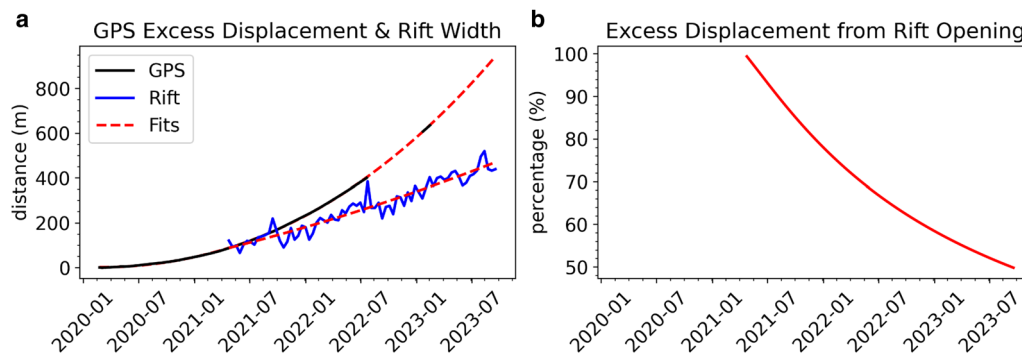


**Figure 10.** Strain relief by rift opening. (a) Lagrangian along-flow distance, obtained from our Cavity Camp GPS record (black line), is compared with the along-flow width of the rift derived from Sentinel-1 SAR imagery (blue line). The red dashed lines depict polynomial fits to mitigate uncertainty in manual picking and extrapolate the GPS record. (b) Notably, the rift opening along the grounding zone completely accommodated the 100 m additional displacement experienced by the ice shelf in April 2021.

Filchner Ice Shelf, could enhance accuracy of the remote sensing, considering that our analysis showed significant acceleration in this area.

Our long-term ApRES data obtained from Cavity Camp also hint at the mechanisms driving melt beneath the Eastern Ice Shelf. Despite low local basal melt rates at this site ( $0.13 \text{ m a}^{-1}$ ), short-term fluctuations in basal melting primarily occur at diurnal tidal frequencies and are closely associated with the 14 d spring–neap tidal cycle (Fig. 4c), despite the region experiencing weak tidal forcing. We attribute this observed signal to the generally uneven basal topography beneath Cavity Camp, which might promote the intermittent development of near-boundary turbulence during spring tides, when compared to other sites located over flatter basal topography.

Basal melting increases non-linearly with depth, as indicated by ApRES measurements (Fig. 3d). The intrusion of thicker ice into deeper ocean waters generally enhances the availability of heat for ice-shelf melting. Modeling studies (e.g. Seroussi and others, 2017) have predicted that ice-shelf thinning is likely to remove the Thwaites Eastern Ice Shelf from deeper ocean heat sources and slow basal melt, at least temporarily. Melt rates for the thinner ice in the inner region were more sensitive to ice thickness than those in the outer region, which might indicate that the ice draft in the inner region is generally closer to the boundary between relatively warm, deeper water and cold, ice-shelf water.

Borehole measurements near the grounding zone of the Thwaites Eastern Ice Shelf highlighted a strongly stratified water column beneath the ice–ocean interface (Davis and others, 2023; Schmidt and others, 2023). This strong stratification is formed by the presence of cold, low-salinity waters accumulated in a 2 m thick layer. Additionally, the low background current speeds are not energetic enough to break the stratification through shear-driven turbulent mixing, which restricts the vertical heat exchange between denser and warmer ocean waters at depth and the ice base. Consequently, as Davis and others (2023) found, measured basal melt rates around the borehole are lower than modeled values that overlook this stratification. Our ApRES survey on the Thwaites Eastern Ice Shelf indicates low-to-moderate basal melt rates, suggesting a widespread presence of the strongly stratified layer observed at the grounding zone (Davis and others, 2023, Fig. 5c). However, fluctuations at tidal frequencies (Fig. 4), although small, suggest that stratification may be periodically disrupted by tidal currents, causing intermittent melt.

#### 4.2 From melting expectations to fracturing reality

Despite relatively consistent and slow rates of basal melt, the destabilization of the Thwaites Eastern Ice Shelf has accelerated.

This is evidenced by the rapid increase in ice-flow speed since 2020, the formation and expansion of fractures in several locations, and the retreat of both the eastern and western calving fronts through calving of icebergs.

##### 4.2.1 Observational insights

We employed Sentinel-1 to observe the temporal and spatial evolution of fracture patterns since 2014. Although visible surface features in the early Sentinel-1 record primarily resulted from past interactions with the Western Glacier Tongue (Alley and others, 2021), a shift occurred in early 2016 during the latest acceleration of the remnants of the Western Glacier Tongue (Miles and others, 2020). At this time, large rifts began to propagate from the shear zone upstream of the pinning point through the central region of the ice shelf. Notably, several of these rifts experienced distinct rapid propagation events during austral spring over 3 consecutive years, followed by the emergence and progression of new rifts in the subsequent 2 years (Fig. 1). It is unclear why these rifts propagated seasonally. We investigated the potential influence of sea ice by comparing records of landfast sea-ice area and sea-ice extent obtained from the US National Ice Center Antarctic Sea Ice Charts (U.S. National Ice Center, 2022) with the timeseries of rift propagation. Despite instances of sea-ice breakout events at the terminus of the Eastern Ice Shelf and Western Glacier Tongue, they did not align temporally with the observed propagation events during austral spring. Furthermore, our GPS-derived ice-speed measurements at Cavity Camp did not reveal coincident short-term acceleration in the central ice-shelf area since their installation in December 2019. Instead, the acceleration of the ice shelf increased continuously, but non-linearly (Fig. 10a). We suggest that this seasonal fracture propagation would form a valuable test case for models of rift propagation, which is beyond the scope of this paper.

We note that propagation of these rifts concludes toward the central ice-shelf region surrounding Cavity Camp, where our ApRES measurements reveal a vertical thickening of the ice column (Fig. 3d). Such ice-column thickening, without basal refreezing, is feasible only in a horizontally compressional regime that restricts further rift propagation. Ice-column thickening was observed at Cavity Camp and nearby sites in January 2020 (Fig. 3d). Since the measurement window was limited, with an average repeat interval of 12 d between ApRES re-visits, the measured strain thickening may be sporadic or related to seasonal strain variations. We further analyze the Cavity Camp strain rate record, which initially showed thickening from January 2020 onward, influenced by the fortnightly spring–neap tidal cycle (Fig. 4d). However, after the January 2022 re-installation of ApRES, the fortnightly tidal influence on the strain thickening

signal only appeared briefly at the beginning of the record and fell below the 5% significance level thereafter. The continuation of the fortnightly modulated diurnal basal melt pattern throughout both ApRES records at Cavity Camp (Fig. 4c), which is fading in its strain-rate record (Fig. 4e), supports the hypothesis that Cavity Camp moved from a strain-thinning to a strain-thickening regime.

At Cavity Camp, the vertical strain pattern exhibits a distinctive question-mark shape with depth below the ice-shelf surface. It shows rapid thickening of the ice column below a 50 m firn layer, followed by rapid thinning in the upper portion, and a trend of slow thinning in the lower half of the ice column (see Fig. 5b). Our interpretation of the upper portion suggests compression, a 30 m thick neutral layer within the ice, and subsequent extension toward the midsection of the ice column. This strain pattern would be characteristic of a sagging beam around a neutral layer. Cavity Camp is located in a surface depression between two sections of thicker ice keels in up- and downstream directions. These keels tend to rotate to maintain hydrostatic equilibrium as the ice shelf spreads out in the along-flow direction. The ApRES 'question-mark' indicates that the tops of the keels move toward each other, leading to horizontal compression of the near surface layers (seen as thickening near the top in ApRES), followed by a near neutral layer and a subsequent layer of horizontal extension (seen as thinning with ApRES). We attribute the weak gradient observed in the lower portion of the ice column to the presence of a nearby basal crevasse, which was observed in nearby ground-penetrating radar, providing localized stress relief to the ice-shelf base. The DTS profile reveals a distinct temperature change from  $-19^{\circ}\text{C}$  at 180 m depth below the ice-shelf surface to  $-1.5^{\circ}\text{C}$  at the ice-ocean interface (Fig. 5c). This temperature reversal corresponds to the initiation of a neutral layer in the bottom half of the ice column, as indicated by ApRES measurements (Fig. 5b). If the opening of a nearby basal crevasse is causing the observed weak strain profile at this depth, it suggests that basal crevassing has likely penetrated nearly halfway through the ice column into the cold core of the ice shelf. Continued penetration toward the ice-shelf surface is facilitated by a predominantly extensional regime at depths between 130 and 180 m, leading to warming ice and reduced viscosity as the basal crevasse penetrates toward the ice-shelf surface.

#### 4.2.2 Why the Thwaites Eastern Ice Shelf is fracturing?

Our observations reveal that fractures tend to originate in high-strain bands and regions with elevated accumulated damage. Notably, these high-strain bands exhibit increased damage levels 1–2 years before surface crevassing becomes observable, though due to vertical averaging and horizontal long-wavelength approximations, the term 'damage' is interpreted as indicative of the ice's predisposition to crevasse formation, rather than literal crevasses. Despite observing crevasses in certain regions, the generally low magnitude of damage (usually  $<0.2$ ) suggests a broader context of weakness, highlighting areas prone to structural vulnerabilities and potential expansion.

Along the three modeled flowlines, we identify concentrated areas where high-strain bands and surface crevassing overlap, particularly near former grounding-zone locations. These high-strain bands are influenced by both ice-surface topography and overall driving stress, which result from undulations in the bed. In regions with steep ice surfaces, increased driving stress leads to faster ice flow, forming localized bands with high-strain rates (Muto and others, 2019). Our observations support a causal link between the bands observable on the ice surface and the bed undulation (Fig. 7). Bumps in the undulation cause compression upstream and extension downstream, which gradually fades until the next bump appears  $\sim 5$ – $10$  km farther downstream. High-strain bands become more visible as the ice speed increases

toward the floating ice. Since these bands also align with past and present grounding-zone locations (Figs 7–9), we suggest they will also play a crucial role in determining future grounding-zone locations as Thwaites Glacier retreats farther inland. We therefore note that grounding-zone retreat will not occur steadily but rather episodically between bumps in the bed.

Our damage modeling integrates melting as a factor contributing to thinning ice and accumulating damage, assuming uniform melt distribution within and outside basal crevasses. This process erodes healthy ice and augments damage (Bassis and Ma, 2015). While recent research indicates differences in melt rates within crevasses compared to the background rates (Washam and others, 2023), our modeling results imply that melt rates have a negligible impact on the large-scale damage evolution of the Thwaites Eastern Ice Shelf (Fig. S4). This highlights the importance of the prevailing dynamical regime. The damage modeling matches the timeline of the ice shelf's fragmentation and shows that dynamic processes have a greater impact on ice-column thinning than basal melt rates. It also illustrates that visible surface crevasses are the result of dynamic processes that began years earlier.

The Thwaites Eastern Ice Shelf experiences fracturing due to several reasons. First, the pinning point continues to weaken as both the width of the compression zone along the flowline and the magnitude of compression decrease over time (Fig. 9c). Our damage modeling shows that, at the same time as compressional stresses from the pinning point weaken, damage increases continuously. This observation aligns with Wild and others (2022) and the results of Benn and others (2022), who showcased a progressive loss of height above flotation and traction over the eastern part of the pinning point since 2015, respectively. Our results align with these findings because they both highlight the impact of the prevailing dynamical regime on the ice shelf's structural changes, corroborating the observed trends in height and traction loss. Second, the emergence of a series of five rifts in the central part of the Thwaites Eastern Ice Shelf coincides with a peak in the velocity of the adjacent remnants of the Western Glacier Tongue in 2016 (Miles and others, 2020). This acceleration increased the stress and strain on the ice shelf, particularly along the shear margin where the ice tongue and the shelf were still connected. The heightened dynamic forces during this period likely contributed to the accumulation of damage and the subsequent formation of these rifts. Expanding our damage calculation beyond the computation along flowlines to encompass transverse strain rates could offer a more comprehensive insight into other factors influencing the opening of rifts at specific times and locations. Third, the emergence of both the grounding-line rift and gash coincided with the swift acceleration of the Eastern Ice Shelf from 2020 onward. While rifting along the grounding zone temporarily accommodated 100% of the observed ice-shelf acceleration in April 2021, the ice shelf continued to accelerate disproportionately until September 2023 (Fig. 10b). Consequently, we expect the occurrence of additional grounding-zone rifts upstream of the current location in the near future.

#### 4.2.3 Comparison to satellite-derived crevasse fields

There has been growing attention to automated mapping of the location and orientation of surface crevasses to assess the vulnerability of ice shelves using publicly available optical and SAR satellite imagery (Lai and others, 2020; Izeboud and Lhermitte, 2023; Surawy-Stepney and others, 2023). Izeboud and Lhermitte (2023), for example, applied their Normalized Radon Transform Damage (NeRD) detection algorithm to the Amundsen Sea Embayment and identified considerable damage signals in the former shear margin between the Thwaites Eastern Ice Shelf and the remnants of the Thwaites Western Glacier Tongue during the austral summer of 2020/21. Here, numerous loose icebergs, bound together

by ice melange, are draining freely into the ocean (see Fig. 8d in Izeboud and Lhermitte, 2023). Within the Thwaites Eastern Ice Shelf, they identified areas such as the crevasse swarm (Fig. 1a), the blue rift (Fig. 1c) and the iceberg rift originating in March 2017 (feature I in Fig. 2b), although the NeRD algorithm tended to underestimate their lengths, particularly at the tips where feature I was penetrating into the basal channel and the blue rift extended farther into the Central Eastern Ice Shelf in 2020/21. This underestimation is likely due to lower image contrast from snow cover, and the challenging ratio of pixel resolution to the decreasing width of these rifts toward their tips.

In contrast, our damage modeling focuses on the dynamic evolution of individual features such as the grounding-zone rift (feature XII in Fig. 8) and the opening gash (feature XVI in Fig. 9), capturing the accumulation of damage along specific flowlines. However, it does not yet offer the broad regional overview provided by image classification algorithms. The strength of these algorithms lies in their ability to capture regional damage states, demonstrating their potential to inform damage model initializations and evaluate ice-sheet models on a larger scale. Nonetheless, to fully monitor the evolution of individual rifts, as highlighted in our study, the algorithms would benefit from higher spatial resolution satellite imagery. Future advances in publicly available satellite technology are expected to enhance multi-source damage detection algorithms like NeRD, improving their capability to capture the evolution of individual features and furthering our understanding of ice-shelf dynamics.

#### 4.3 Opening gash as a window for future ice cliff at present-day grounding zone?

Our observations of rifts and gashes along the grounding zone imply that the Thwaites Eastern Ice Shelf has largely detached from its tributary glacier. The widening of the gash supports the notion that the ice shelf no longer exerts substantial back-stress on Thwaites Glacier, consistent with the findings of Gudmundsson and others (2023). However, the presence of the ice shelf may still have an indirect influence on glacier dynamics. Observations and simple force balance calculations elsewhere, e.g. Jakobshavn Isbræ (Amundson and others, 2010), indicate that the presence of an ice shelf or an ice melange can significantly affect the calving style by preventing the overturning and evacuation of large icebergs, which then affects the terminal extent of the grounding zone and hence glacier dynamics. It is therefore plausible that, even beyond the final breakup of the ice shelf, its past presence will continue to significantly influence the future of Thwaites Glacier.

## 5. Conclusion

Minimal basal melting occurs beneath the Thwaites Eastern Ice Shelf, despite the presence of ample oceanic heat at depth. This observation suggests that the well-defined stratification of ocean water beneath the ice–ocean interface, as observed at the grounding zone (Davis and others, 2023; Schmidt and others, 2023), extends to the broader ice-shelf region (e.g. Dotto and others, 2022). The moderate melting that does happen is correlated with ice-shelf thickness, with thicker ice (~400 m) experiencing relatively faster melting compared to thinner ice (~300 m). The ongoing evolution of several rifts penetrating the central part of the ice shelf has surpassed the rate of basal melting. While these rifts previously exhibited rapid propagation events, they appeared to have largely become inactive in 3 years since the last major advancement in the austral summer of 2021/22. Nevertheless, their threshold-like behavior carries the potential to trigger a rapid collapse of the ice shelf should they reactivate. This has become increasingly probable with the recent activation

of the Thwaites Eastern Ice Shelf's western calving front, following the breakout of sea ice in the former shear margin with the adjacent the Thwaites Western Glacier Tongue.

Farther upstream, the ongoing rifting at the retreating grounding zone has briefly accommodated the 70% ice-flow acceleration since December 2019. As a result of these full-thickness rifts, the ice shelf has almost completely separated from its tributary ice stream and now exists as a thin, floating ice plate, offering minimal support to the grounded sections of Thwaites Glacier. The emergence of full-thickness rifts and gashes provides valuable insights into the anticipated dynamics of a likely new calving front that has already been observed to the west of Thwaites Glacier's main trunk, where capsizing icebergs have been steadily calving off at least since the launch of Sentinel-1 in 2014. These observations show that, while ocean forcing is responsible for triggering the current retreat of West Antarctica, the Thwaites Eastern Ice Shelf is experiencing dynamic feedbacks toward the end of its life that are driving ice-shelf disintegration independent of basal melt.

**Supplementary material.** The supplementary material for this article can be found at <https://doi.org/10.1017/jog.2024.64>.

**Data.** The ApRES and DTS data will be accessible through the USAP-DC upon acceptance of this article (<https://www.usap-dc.org/view/project/p0010162>). Sentinel-1 imagery is available from the Copernicus Open Access Hub (<https://scihub.copernicus.eu/>). Velocity fields from Sentinel-1 are available from A.L. Picks of rifts and other surface features are available from C.T.W. Python code for modeling damage along flowlines will be accessible through S.B.K.'s GitHub account. All other data sources mentioned in this study are detailed within the text.

**Acknowledgments.** We express our gratitude to the field team members, including Bruce Wallin, Douglas Fox, Dale Pomraning, Blair Fyffe, Cece Mortensen (2019/20 season) and Kira Solomon with Chris Simmons (2021/22 season), for their dedicated fieldwork efforts. We thank the EarthScope Consortium and particularly Nicolas Bayou for their technical support. We also acknowledge the invaluable support from the work centers at McMurdo, the WAIS Divide staff and Kenn Borek Air. Special thanks to Kelsey Mark Kushneryk and Jeff Amantea for their unwavering commitment during the challenging COVID season in 2021/22. We thank Eric Rignot for providing InSAR-derived grounding zones. C.T.W. acknowledges valuable discussions with TJ Young regarding ApRES processing. Sentinel-1 data were provided by the EU Copernicus Programme. We thank Frank Pattyn for his valuable contributions, including editing and handling this paper, as well as stepping up as a reviewer and providing a second review alongside one other anonymous reviewer. We acknowledge support by Open Access Publishing Fund of University of Tübingen. This research is from the TARSAN and DOMINOS projects, components of the International Thwaites Glacier Collaboration (ITGC). Support is received from National Science Foundation (NSF: grant 1929991) and the Natural Environment Research Council (NERC: grant NE/S006419/1). Logistics provided by NSF-US Antarctic Program and NERC-British Antarctic Survey is acknowledged. ITGC Contribution No. ITGC-123.

**Author contributions.** C.T.W. conceived the study, led data analysis and drafted the manuscript. S.B.K. conducted damage modeling experiments. A.L. and S.L.B. produced velocity fields from Sentinel-1. K.E.A. and M.T. contributed to interpretation of Hovmöller diagrams and also contributed to writing. C.T.W., M.A.S. and H.S. picked features in SAR imagery. M.T. processed GPS data. S.W.T., T.S.D. and C.K. calibrated and processed DTS data. K.W.N. assisted with ApRES data processing. D.P. assisted with interpretation of SAR data. T.A.S. led 2021/22 fieldwork. G.C.-B. and A.M. contributed to fieldwork. E.C.P. and K.J.H. were principal investigators of the TARSAN project. All authors discussed results, implications, provided feedback and approved of the final manuscript.

## References

- Adusumilli S, Fricker HA, Medley B, Padman L and Siegfried MR (2020) Interannual variations in meltwater input to the Southern Ocean from Antarctic ice shelves. *Nature Geoscience* 13(9), 616–620. doi: [10.1038/s41561-020-0616-z](https://doi.org/10.1038/s41561-020-0616-z)



- Alley KE and 10 others (2021) Two decades of dynamic change and progressive destabilization on the Thwaites Eastern Ice Shelf. *The Cryosphere*, 15(11), 5187–5203. doi: [10.5194/tc-15-5187-2021](https://doi.org/10.5194/tc-15-5187-2021)
- Alley KE, Scambos TA and Alley RB (2023) The role of channelized basal melt in ice-shelf stability: recent progress and future priorities. *Annals of Glaciology* 63(87–89), 18–22. doi: [10.1017/aog.2023.5](https://doi.org/10.1017/aog.2023.5)
- Amundson JM and 5 others (2010) Ice mélange dynamics and implications for terminus stability, Jakobshavn Isbræ, Greenland. *Journal of Geophysical Research: Earth Surface* 115(F01005). doi: [10.1029/2009JF001405](https://doi.org/10.1029/2009JF001405)
- Bassis JN and Ma Y (2015) Evolution of basal crevasses links ice shelf stability to ocean forcing. *Earth and Planetary Science Letters* 409, 203–211. doi: [10.1016/j.epsl.2014.11.003](https://doi.org/10.1016/j.epsl.2014.11.003)
- Benn DI and 10 others (2022) Rapid fragmentation of Thwaites Eastern Ice Shelf. *The Cryosphere* 16(6), 2545–2564. doi: [10.5194/tc-16-2545-2022](https://doi.org/10.5194/tc-16-2545-2022)
- Borstad C and 5 others (2016) A constitutive framework for predicting weakening and reduced buttressing of ice shelves based on observations of the progressive deterioration of the remnant Larsen B Ice Shelf. *Geophysical Research Letters* 43(5), 2027–2035. doi: [10.1002/2015gl067365](https://doi.org/10.1002/2015gl067365)
- Brennan PV, Lok LB, Nicholls KW and Corr HF (2014) Phase-sensitive FMCW radar system for high-precision Antarctic ice shelf profile monitoring. *IET Radar, Sonar & Navigation* 8(7), 776–786. doi: [10.1049/iet-rsn.2013.0053](https://doi.org/10.1049/iet-rsn.2013.0053)
- Clark RW and 10 others (2024). Synchronous retreat of Thwaites and Pine Island glaciers in response to external forcings in the presatellite era. *Proceedings of the National Academy of Sciences*, 121(11), e2211711120. doi: [10.1073/pnas.2211711120](https://doi.org/10.1073/pnas.2211711120)
- Corr HF, Jenkins A, Nicholls KW and Doake CSM (2002) Precise measurement of changes in ice-shelf thickness by phase-sensitive radar to determine basal melt rates. *Geophysical Research Letters* 29(8), 73–71. doi: [10.1029/2001GL014618](https://doi.org/10.1029/2001GL014618)
- Crawford AJ and 5 others (2021) Marine ice-cliff instability modeling shows mixed-mode ice-cliff failure and yields calving rate parameterization. *Nature Communications*, 12(1), 2701. doi: [10.1038/s41467-021-23070-7](https://doi.org/10.1038/s41467-021-23070-7)
- Davis PE and 10 others (2023) Suppressed basal melting in the eastern Thwaites Glacier grounding zone. *Nature* 614(7948), 479–485. doi: [10.1038/s41586-022-05586-0](https://doi.org/10.1038/s41586-022-05586-0)
- Dotto TS and 10 others (2022) Ocean variability beneath Thwaites Eastern Ice Shelf driven by the Pine Island Bay Gyre strength. *Nature Communications* 13(1), 7840. doi: [10.1038/s41467-022-35499-5](https://doi.org/10.1038/s41467-022-35499-5)
- Fretwell P and 10 others (2013) Bedmap2: improved ice bed, surface and thickness datasets for Antarctica. *The Cryosphere* 7(1), 375–393. doi: [10.5194/tc-7-375-2013](https://doi.org/10.5194/tc-7-375-2013)
- Grinsted A, Moore, JC and Jevrejeva, S (2004) Application of the cross wavelet transform and wavelet coherence to geophysical time series. *Nonlinear Processes in Geophysics* 11(5/6), 561–566. doi: [10.5194/npg-11-561-2004](https://doi.org/10.5194/npg-11-561-2004)
- Gudmundsson GH (2013) Ice-shelf buttressing and the stability of marine ice sheets. *The Cryosphere*, 7(2), 647–655. doi: [10.5194/tc-7-647-2013](https://doi.org/10.5194/tc-7-647-2013)
- Gudmundsson GH, Barnes JM, Goldberg DN and Morlighem, M (2023) Limited impact of Thwaites Ice Shelf on future ice loss from Antarctica. *Geophysical Research Letters*, 50(11), e2023GL102880. doi: [10.1029/2023GL102880](https://doi.org/10.1029/2023GL102880)
- Herring TA, King RW, Floyd MA and McClusky SC (2018) Introduction to GAMIT/GLOBK, Release 10.71. Department of Earth, Atmospheric, and Planetary Sciences, Massachusetts Institute of Technology, Cambridge, MA. 54 pp. Available at <http://geoweb.mit.edu/gg/>
- Hillenbrand CD and 10 others (2017) West Antarctic Ice Sheet retreat driven by Holocene warm water incursions. *Nature* 547(7661), 43–48. doi: [10.1038/nature22995](https://doi.org/10.1038/nature22995)
- Howard SL, Erofeeva S and Padman L (2019) ‘CATS2008: Circum-Antarctic Tidal Simulation version 2008’ U.S. Antarctic Program (USAP) Data Center. doi: [10.15784/601235](https://doi.org/10.15784/601235)
- Howat IM, Porter C, Smith BE, Noh MJ and Morin P (2019) The reference elevation model of Antarctica. *The Cryosphere* 13(2), 665–674. doi: [10.5194/tc-13-665-2019](https://doi.org/10.5194/tc-13-665-2019)
- Izeboud M and Lhermitte S (2023) Damage detection on Antarctic ice shelves using the normalised radon transform. *Remote Sensing of Environment* 284, 113359. doi: [10.1016/j.rse.2022.113359](https://doi.org/10.1016/j.rse.2022.113359)
- Jenkins A and 7 others (2018) West Antarctic Ice Sheet retreat in the Amundsen Sea driven by decadal oceanic variability. *Nature Geoscience* 11(10), 733–738. doi: [10.1038/s41561-018-0207-4](https://doi.org/10.1038/s41561-018-0207-4)
- Joughin I, Smith BE and Medley B (2014) Marine ice sheet collapse potentially under way for the Thwaites Glacier Basin, West Antarctica. *Science* 344(6185), 735–738. doi: [10.1126/science.1249055](https://doi.org/10.1126/science.1249055)
- Kachuck SB, Martin DF, Bassis JN and Price SF (2020) Rapid viscoelastic deformation slows marine ice sheet instability at Pine Island Glacier. *Geophysical Research Letters* 47(10), e2019GL086446. doi: [10.1029/2019GL086446](https://doi.org/10.1029/2019GL086446)
- Kachuck SB, Whitcomb M, Bassis JN, Martin DF and Price SF (2022) Simulating ice-shelf extent using damage mechanics. *Journal of Glaciology* 68(271), 987–998. doi: [10.1017/jog.2022.12](https://doi.org/10.1017/jog.2022.12)
- Konrad H and 6 others (2018) Net retreat of Antarctic Glacier grounding lines. *Nature Geoscience* 11(4), 258–262. doi: [10.1038/s41561-018-0082-z](https://doi.org/10.1038/s41561-018-0082-z)
- Lai CY and 7 others (2020). Vulnerability of Antarctica’s ice shelves to meltwater-driven fracture. *Nature* 584(7822), 574–578. doi: [10.1038/s41586-020-2627-8](https://doi.org/10.1038/s41586-020-2627-8)
- Lhermitte S and 7 others (2020) Damage accelerates ice shelf instability and mass loss in Amundsen Sea Embayment. *Proceedings of the National Academy of Sciences* 117(40), 24735–24741. doi: [10.1073/pnas.1912890117](https://doi.org/10.1073/pnas.1912890117)
- Luckman, A and 5 others (2015) Calving rates at tidewater glaciers vary strongly with ocean temperature. *Nature Communications*, 6, 8566. doi: [10.1038/ncomms9566](https://doi.org/10.1038/ncomms9566)
- MacGregor JA, Catania GA, Markowski MS and Andrews AG (2012) Widespread rifting and retreat of ice-shelf margins in the eastern Amundsen Sea Embayment between 1972 and 2011. *Journal of Glaciology*, 58(209), 458–466. doi: [10.3189/2012JG11J262](https://doi.org/10.3189/2012JG11J262)
- Miles BWJ and 5 others (2020) Intermittent structural weakening and acceleration of the Thwaites Glacier Tongue between 2000 and 2018. *Journal of Glaciology* 66(257), 485–495. doi: [10.1017/jog.2020.20](https://doi.org/10.1017/jog.2020.20)
- Milillo P and 6 others (2019) Heterogeneous retreat and ice melt of Thwaites Glacier, West Antarctica. *Science Advances* 5(1), eaau3433. doi: [10.1126/sciadv.aau3433](https://doi.org/10.1126/sciadv.aau3433)
- Morlighem M (2022) MEaSUREs BedMachine Antarctica, Version 3 [Data Set]. Boulder, Colorado, USA. NASA National Snow and Ice Data Center Distributed Active Archive Center. doi: [10.5067/FPSU0V1MWUB6](https://doi.org/10.5067/FPSU0V1MWUB6)
- Morlighem M and 5 others (2020) Deep glacial troughs and stabilizing ridges unveiled beneath the margins of the Antarctic ice sheet. *Nature Geoscience* 13, 132–137. doi: [10.1038/s41561-019-0510-8](https://doi.org/10.1038/s41561-019-0510-8)
- Muto, Alley RB, Parizek BR and Anandakrishnan S (2019) Bed-type variability and till (dis)continuity beneath Thwaites Glacier, West Antarctica. *Annals of Glaciology* 60(80), 82–90. doi: [10.1017/aog.2019.32](https://doi.org/10.1017/aog.2019.32)
- Nicholls KW and 5 others (2015) A ground-based radar for measuring vertical strain rates and time-varying basal melt rates in ice sheets and shelves. *Journal of Glaciology* 61(230), 1079–1087. doi: [10.3189/2015JG15J073](https://doi.org/10.3189/2015JG15J073)
- Padman L, Fricker HA, Coleman R, Howard S and Erofeeva L (2002) A new tide model for the Antarctic ice shelves and seas. *Annals of Glaciology* 34, 247–254. doi: [10.3189/172756402781817752](https://doi.org/10.3189/172756402781817752)
- Paolo FS, Fricker HA and Padman L (2015) Volume loss from Antarctic ice shelves is accelerating. *Science*, 348(6232), 327–331. doi: [10.1126/science.aaa0940](https://doi.org/10.1126/science.aaa0940)
- Pollard D, DeConto RM and Alley RB (2015) Potential Antarctic Ice Sheet retreat driven by hydrofracturing and ice cliff failure. *Earth and Planetary Science Letters* 412, 112–121. doi: [10.1016/j.epsl.2014.12.035](https://doi.org/10.1016/j.epsl.2014.12.035)
- Pritchard HD, Arthern RJ, Vaughan DG and Edwards LA (2009) Extensive dynamic thinning on the margins of the Greenland and Antarctic ice sheets. *Nature* 461(7266), 971–975. doi: [10.1038/nature08471](https://doi.org/10.1038/nature08471)
- Pritchard HD and 5 others (2012) Antarctic ice-sheet loss driven by basal melting of ice shelves. *Nature* 484(7395), 502–505. doi: [10.1038/nature10968](https://doi.org/10.1038/nature10968)
- Rack W and Rott H (2004) Pattern of retreat and disintegration of the Larsen B Ice Shelf, Antarctic Peninsula. *Annals of Glaciology* 39, 505–510. doi: [10.3189/172756404781814005](https://doi.org/10.3189/172756404781814005)
- Scambos TA, Bohlander JA, Shuman CA and Skvarca P (2004) Glacier acceleration and thinning after ice shelf collapse in the Larsen B Embayment, Antarctica. *Geophysical Research Letters* 31(18), L18402. doi: [10.1029/2004GL020670](https://doi.org/10.1029/2004GL020670)
- Scambos TA, Behar A, Ross R and Stroev J (2013) New pathfinder technology for ice–ocean system monitoring. *Proceedings of Arctic Observing Summit*, Vancouver, BC, Canada, 30 April–2 May.
- Schmidt BE and 10 others (2023) Heterogeneous melting near the Thwaites Glacier grounding line. *Nature* 614(7948), 471–478. doi: [10.1038/s41586-022-05691-0](https://doi.org/10.1038/s41586-022-05691-0)
- Schmidtko S, Heywood KJ, Thompson AF and Aoki S (2014) Multidecadal warming of Antarctic waters. *Science* 346(6214), 1227–1231. doi: [10.1126/science.1256117](https://doi.org/10.1126/science.1256117)
- Seabold S and Perktold J (2010) Statsmodels: econometric and statistical modeling with Python. *Proceedings of the 9th Python in Science Conference (SciPy 2010)*, Austin, TX, USA, 28 June–3 July 2010, pp. 57–61. doi: [10.25080/Majora-92bf1922-011](https://doi.org/10.25080/Majora-92bf1922-011)

- Seroussi H and 6 others** (2017) Continued retreat of Thwaites Glacier, West Antarctica, controlled by bed topography and ocean circulation. *Geophysical Research Letters* **44**(12), 6191–6199. doi: [10.1002/2017GL072910](https://doi.org/10.1002/2017GL072910)
- Shepherd A, Wingham D and Rignot E** (2004) Warm ocean is eroding West Antarctic ice sheet. *Geophysical Research Letters* **31**(23), L23402. doi: [10.1029/2004GL021106](https://doi.org/10.1029/2004GL021106)
- Smith JA and 10 others** (2017) Sub-ice-shelf sediments record history of twentieth-century retreat of Pine Island Glacier. *Nature* **541**(7635), 77–80. doi: [10.1038/nature20136](https://doi.org/10.1038/nature20136)
- Steig EJ and 10 others** (2013) Recent climate and ice-sheet changes in West Antarctica compared with the past 2,000 years. *Nature Geoscience* **6**(5), 372–375. doi: [10.1038/ngeo1778](https://doi.org/10.1038/ngeo1778)
- Sun S, Cornford SL, Moore JC, Gladstone R and Zhao L.** (2017) Ice shelf fracture parameterization in an ice sheet model. *The Cryosphere* **11**, 2543–2554. doi: [10.5194/tc-11-2543-2017](https://doi.org/10.5194/tc-11-2543-2017)
- Surawy-Stepney T, Hogg AE, Cornford SL and Davison BJ** (2023) Episodic dynamic change linked to damage on the Thwaites Glacier Ice Tongue. *Nature Geoscience* **16**(1), 37–43. doi: [10.1038/s41561-022-01097-9](https://doi.org/10.1038/s41561-022-01097-9)
- Sutterley TC and 7 others** (2014) Mass loss of the Amundsen Sea Embayment of West Antarctica from four independent techniques. *Geophysical Research Letters* **41**(23), 8421–8428. doi: [10.1002/2014GL061940](https://doi.org/10.1002/2014GL061940)
- Tinto KJ and Bell RE** (2011) Progressive unpinning of Thwaites Glacier from newly identified offshore ridge: constraints from aerogravity. *Geophysical Research Letters* **38**(20), L20503. doi: [10.1029/2011GL049026](https://doi.org/10.1029/2011GL049026)
- U.S. National Ice Center** (2022) U.S. National Ice Center Arctic and Antarctic Sea Ice Charts in SIGRID-3 Format, Version 1 [Data Set]. Boulder, Colorado, USA. National Snow and Ice Data Center. doi: [10.7265/4b7s-rn93](https://doi.org/10.7265/4b7s-rn93). Accessed 12 May 2023.
- van der Walt S and 7 others** (2014). scikit-image: image processing in Python. *PeerJ* **2**, e453. doi: [10.7717/peerj.453](https://doi.org/10.7717/peerj.453)
- Vaňková I, Nicholls KW, Corr HF, Makinson K and Brennan PV** (2020) Observations of tidal melt and vertical strain at the Filchner-Ronne Ice Shelf, Antarctica. *Journal of Geophysical Research: Earth Surface* **125**(1), e2019JF005280. doi: [10.1029/2019JF005280](https://doi.org/10.1029/2019JF005280)
- Wählin AK and 8 others** (2021) Pathways and modification of warm water flowing beneath Thwaites Ice Shelf, West Antarctica. *Science Advances* **7**(15), eabd7254. doi: [10.1126/sciadv.abd7254](https://doi.org/10.1126/sciadv.abd7254)
- Washam P and 10 others** (2023) Direct observations of melting, freezing, and ocean circulation in an ice shelf basal crevasse. *Science Advances* **9**(43), eadi7638. doi: [10.1126/sciadv.adi7638](https://doi.org/10.1126/sciadv.adi7638)
- Whitaker J and 6 others** 'Jswit/pyproj: Version 2.0.2 Release'. Zenodo, 13 March 2019. doi: [10.5281/zenodo.2592233](https://doi.org/10.5281/zenodo.2592233)
- Wild CT and 5 others** (2021) 'Thwaites Glacier grounding lines for 2014 and 2019/20 from height above flotation', U.S. Antarctic Program (USAP) Data Center. doi: [10.15784/601499](https://doi.org/10.15784/601499)
- Wild CT and 5 others** (2022) Weakening of the pinning point buttressing Thwaites Glacier, West Antarctica. *The Cryosphere*, **16**(2), 397–417. doi: [10.5194/tc-16-397-2022](https://doi.org/10.5194/tc-16-397-2022)
- Zeising O and 5 others** (2022) Basal melt of the southern Filchner Ice Shelf, Antarctica. *The Cryosphere* **16**(4), 1469–1482. doi: [10.5194/tc-16-1469-2022](https://doi.org/10.5194/tc-16-1469-2022)